



Dynamic rupture modeling on unstructured meshes using a discontinuous Galerkin method

J. de la Puente,^{1,2} J.-P. Ampuero,³ and M. Käser¹

Received 23 December 2008; revised 23 June 2009; accepted 6 July 2009; published 1 October 2009.

[1] We introduce the application of an arbitrary high-order derivative (ADER) discontinuous Galerkin (DG) method to simulate earthquake rupture dynamics. The ADER-DG method uses triangles as computational cells which simplifies the process of discretization of very complex surfaces and volumes by using external automated tools. Discontinuous Galerkin methods are well suited for solving dynamic rupture problems in the velocity-stress formulation as the variables are naturally discontinuous at the interface between two elements. Therefore, the fault has to be honored by the computational mesh. The so-called Riemann problem can be solved to obtain well defined values of the variables at the discontinuity itself. Fault geometries of high complexity can be modeled thanks to the flexibility of unstructured meshes, which solves a major bottleneck of other high-order numerical methods. Additionally, element refinement and coarsening are easily controlled in the meshing process to better resolve the near-fault area of the model. The fundamental properties of the method are shown, as well as a series of validating exercises with reference solutions and a comparison with the well-established finite difference, boundary integral, and spectral element methods, in order to test the accuracy of our formulation. An example of dynamic rupture on a nonplanar fault based upon the Landers 1992 earthquake fault system is presented to illustrate the main potentials of the new method.

Citation: de la Puente, J., J.-P. Ampuero, and M. Käser (2009), Dynamic rupture modeling on unstructured meshes using a discontinuous Galerkin method, *J. Geophys. Res.*, *114*, B10302, doi:10.1029/2008JB006271.

1. Introduction

[2] Computational earthquake dynamics is emerging as a key component in physics-based approaches to strong motion prediction for seismic hazard assessment, and in physically constrained inversion approaches to earthquake source imaging from seismological and geodetic observations. Typical applications in both areas require the ability to deal with rupture surfaces of complicated, realistic geometries with high computational efficiency. A variety of numerical methods have been used in the past decades to simulate the dynamics of earthquake rupture, as finite differences (FD) [e.g., *Andrews*, 1973; *Day*, 1982; *Madariaga et al.*, 1998; *Andrews*, 1999; *Dalguer and Day*, 2007; *Moczo et al.*, 2007; *Ely et al.*, 2009], finite elements (FE) [e.g., *Oglesby et al.*, 1998, 2000; *Aagaard et al.*, 2001], boundary integral (BI) [e.g., *Das*, 1980; *Andrews*, 1985; *Cochard and Madariaga*, 1994; *Geubelle and Rice*, 1995; *Lapusta et al.*, 2000], spectral element (SE) [*Ampuero*, 2002; *Vilotte et al.*,

2006; *Kaneko et al.*, 2008], or finite volume (FV) [*Benjema et al.*, 2007] methods.

[3] These techniques offer different advantages and drawbacks. The BI method offers very high accuracy and efficiency, but is not well suited for handling heterogeneous media and nonlinear materials. The FD method is very accurate but is difficult to apply to nonplanar faults, with some remarkable exceptions [e.g., *Cruz-Atienza and Virieux*, 2004]. The FE and FV methods are very flexible geometrically but are often implemented as first- to second-order operators that are very dispersive for wave propagation problems. The hexahedra-based SE method is both accurate and flexible, but designing good quality hexahedral meshes for complicated geometries in three dimensions, such as faults with branching, and adapting smoothly the element sizes to different material properties are still very challenging tasks [*Igel et al.*, 2008] and a major bottleneck.

[4] Here, we present an alternative for the computation of the dynamics of two-dimensional in-plane rupture phenomena, based upon a discontinuous Galerkin (DG) method combined with an arbitrary high-order derivatives (ADER) time integration. The DG methods can be thought of as a high-order version of FV methods, where a polynomial basis is used inside each element to represent the unknowns. In our implementation, triangular elements are used which allows for a better fit of the geometrical constraints of the problem, i.e., the fault shape, and for an easy control of the

¹Department of Earth and Environmental Sciences, Ludwig-Maximilians-University, Munich, Germany.

²Now at Institut de Ciències del Mar, CSIC, Barcelona, Spain.

³Seismological Laboratory, California Institute of Technology, Pasadena, USA.

variation of element sizes using smooth refining and coarsening strategies.

[5] The ADER-DG method has been applied to continuous wave propagation problems [Käser and Dumbser, 2006; Dumbser and Käser, 2006], including viscoelastic [Käser et al., 2007a], anisotropic [de la Puente et al., 2007] and poroelastic [de la Puente et al., 2008] rheologies. Also the kinematic description of nonplanar irregular faults has been successfully implemented [Käser et al., 2007b].

[6] A particular feature of DG methods, inherited from FV methods, is the usage of numerical fluxes at element interfaces. Between any two elements the variables of the elastic equations are allowed to be discontinuous, even when no faults are present. This is enabled by the availability of the exact solution to the elastic wave equation at a discontinuity, obtained by the solution of the well-known Riemann problem [Toro, 1999; LeVeque, 2002]. In the case of faults, the solution of the Riemann problem has to be modified to incorporate frictional boundary conditions. Once the Riemann problem is solved, numerical fluxes are used to exchange information between elements.

2. Dynamics of Fault Rupture

[7] Faults are classically described as surfaces (or curves in two dimensions) of tangential displacement discontinuity (slip) on which traction and slip are related by friction [e.g., Andrews, 1976a, 1976b]. In our description of the rupture process, the material surrounding the fault is assumed elastic, so all nonlinearities of the problem are contained in the fault boundary conditions. We confine the presentation to the 2-D in-plane case. Following usual conventions, we call the sides of the fault the positive and negative sides, and define the fault normal vector pointing from the positive toward the negative side. The kinematics of the sliding process can be described by the slip rate $\Delta v = v_t^+ - v_t^-$, where v_t is the velocity parallel to the fault, and the slip Δd , so that $\Delta v = \Delta \dot{d}$. We denote τ and σ the absolute shear and normal stresses on the fault, respectively.

[8] Slip starts when the shear stress on the fault overcomes a certain threshold, the fault strength. In the Coulomb friction model adopted here the strength is proportional to the normal stress. During active slip, the slip rate and the shear traction have opposite directions. These three phenomena are accounted for in the following expressions:

$$\begin{aligned} |\tau| &\leq \mu_f \sigma, \\ (|\tau| - \mu_f \sigma) \Delta v &= 0, \\ \Delta v |\tau| + |\Delta v| \tau &= 0, \end{aligned} \quad (1)$$

where μ_f is the friction coefficient, which generally depends on slip, slip rate and fault state variables. We adopt the linear slip weakening (LSW) friction law [Ida, 1972; Palmer and Rice, 1973]

$$\mu_f = \begin{cases} \mu_s - \frac{\mu_s - \mu_d}{D_c} \Delta d & \text{if } \Delta d < D_c, \\ \mu_d & \text{if } \Delta d \geq D_c. \end{cases} \quad (2)$$

In this expression μ_s , μ_d and D_c are all friction parameters, namely the static friction coefficient, dynamic friction

coefficient and critical slip distance, respectively. This friction law, although simple, is sufficient to describe the initial rupture, arrest of sliding and reactivation of slip. Because of its simplicity, it is commonly used in numerical modeling of earthquake dynamics and in related validation problems. Notice that this friction law has discontinuous derivatives with respect to slip. As a consequence, numerical methods which achieve high-order accuracy using smooth polynomial expansions of the variables might fail to describe with sufficient accuracy those rupture phenomena described with the aforementioned LSW friction.

3. The Riemann Problem for Elastodynamics

[9] Considering two-dimensional elasticity for an isotropic medium in velocity-stress formulation and omitting external sources (e.g., moments or body forces) leads to the elastic wave equation, a linear hyperbolic system of the form

$$\begin{aligned} \frac{\partial}{\partial t} \sigma_{xx} - (\lambda + 2\mu) \frac{\partial}{\partial x} u - \lambda \frac{\partial}{\partial y} v &= 0, \\ \frac{\partial}{\partial t} \sigma_{yy} - \lambda \frac{\partial}{\partial x} u - (\lambda + 2\mu) \frac{\partial}{\partial y} v &= 0, \\ \frac{\partial}{\partial t} \sigma_{xy} - \mu \left(\frac{\partial}{\partial x} v + \frac{\partial}{\partial y} u \right) &= 0, \\ \rho \frac{\partial}{\partial t} u - \frac{\partial}{\partial x} \sigma_{xx} - \frac{\partial}{\partial y} \sigma_{xy} &= 0, \\ \rho \frac{\partial}{\partial t} v - \frac{\partial}{\partial x} \sigma_{xy} - \frac{\partial}{\partial y} \sigma_{yy} &= 0, \end{aligned} \quad (3)$$

where λ is the first Lamé constant, μ is the shear modulus, not to be confused with the friction coefficient μ_f mentioned earlier, and ρ is the mass density of the material. The components of the stress tensor are σ_{xx} , σ_{yy} and σ_{xy} . The components of the particle velocities in x and y direction are denoted by u and v , respectively.

[10] The elastic wave equation requires continuity of the involved variables, i.e., particle velocities and stresses. However, the partial differential equations of (3) can be solved also at variable discontinuities and material discontinuities. An evolution problem with initial values that are piecewise constant, discontinuous across an interface, is called a Riemann problem [Toro, 1999; LeVeque, 2002]. Riemann problems are local, involving only the points immediately contiguous to the discontinuity interface.

[11] Following LeVeque [2002], we group the stress and velocity variables into a vector $\mathbf{Q} = (\sigma_{xx}, \sigma_{yy}, \sigma_{xy}, u, v)^T$ and write the equations (3) in matrix form as

$$\frac{\partial \mathbf{Q}_p}{\partial t} + A_{pq} \frac{\partial \mathbf{Q}_q}{\partial x} + B_{pq} \frac{\partial \mathbf{Q}_q}{\partial y} = 0. \quad (4)$$

The classical tensor notation is adopted, which implies summation over repeated indices. The matrices A_{pq} and B_{pq} are the space-dependent Jacobian matrices, which are given explicitly by Käser and Dumbser [2006].

[12] To illustrate the solution of the Riemann problem for the system (4), we consider an element interface S with a normal that is aligned with the x axis. The corresponding

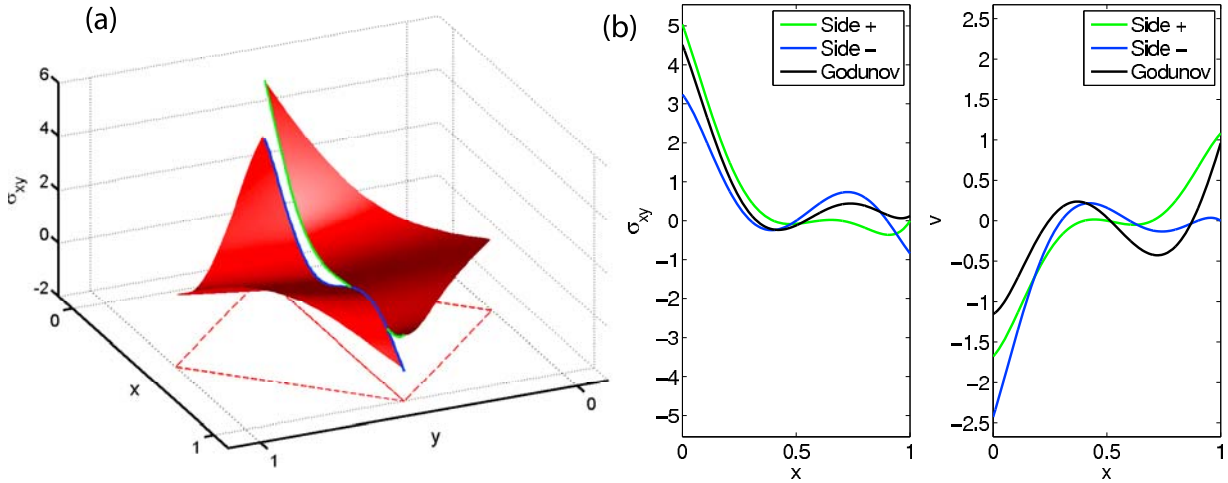


Figure 1. (a) Two triangle-based polynomial representations of the σ_{xy} variable which are discontinuous at their interface situated at $y = 0.5$. (b) The Godunov state of variables σ_{xy} and v at that same interface.

Riemann problem is purely one-dimensional and depends exclusively on the Jacobian matrix A . We suppose two discontinuous initial states at both sides of the interface, \mathbf{Q}^+ and \mathbf{Q}^- , and assume that the material properties are the same on both sides of the interface. The Jacobian matrix A is diagonalized as

$$A_{pq} = R_{pm} \Lambda_{ml} R_{lq}^{-1}, \quad (5)$$

where Λ is a diagonal matrix containing the eigenvalues $\{\lambda_i\}_{i=1,\dots,5}$ of A and R a matrix containing the corresponding right eigenvectors of A . The boundary values on the positive side, $\mathbf{Q}(S^+)$, are obtained as a linear combination of the right eigenvectors associated to the positive eigenvalues, λ_1 and λ_2 , corresponding to P and S waves traveling from the negative side to the positive side:

$$\mathbf{Q}_p(S^+) = \mathbf{Q}_p^+ + \sum_{i=1}^2 \alpha_i R_{pi}. \quad (6)$$

The so-called wave strengths α_i are given by

$$\alpha_i = R_{ij}^{-1} (\mathbf{Q}_j^- - \mathbf{Q}_j^+). \quad (7)$$

Similarly, the boundary values on the negative side, $\mathbf{Q}(S^-)$, are obtained from the eigenvectors associated to the negative eigenvalues, λ_4 and λ_5 :

$$\mathbf{Q}_p(S^-) = \mathbf{Q}_p^- - \sum_{i=4}^5 \alpha_i R_{pi}. \quad (8)$$

In the absence of additional forces both expressions (6) and (8) give the same value, coined the Godunov state:

$$\mathbf{Q}_p^G = \mathbf{Q}_p(S^-) = \mathbf{Q}_p(S^+). \quad (9)$$

The explicit values of all variables in the Godunov state are

$$\begin{aligned} 2\sigma_{xx}^G &= (\sigma_{xx}^- + \sigma_{xx}^+) + \frac{\lambda + 2\mu}{c_p} (u^- - u^+), \\ 2\sigma_{yy}^G &= \frac{\lambda}{c_p} (u^- - u^+) + \frac{\lambda}{\lambda + 2\mu} (\sigma_{xx}^- + \sigma_{xx}^+) + 2\sigma_{yy}^+, \\ 2\sigma_{xy}^G &= (\sigma_{xy}^- + \sigma_{xy}^+) + \frac{\mu}{c_s} (v^- - v^+), \\ 2u^G &= (u^- + u^+) + \frac{c_p}{\lambda + 2\mu} (\sigma_{xx}^- - \sigma_{xx}^+), \\ 2v^G &= (v^- + v^+) + \frac{c_s}{\mu} (\sigma_{xy}^- - \sigma_{xy}^+), \end{aligned} \quad (10)$$

where c_p and c_s are the P and S wave velocities, respectively. Equations (10) show that the Godunov state is the result of applying a bilinear operator to \mathbf{Q}^+ and \mathbf{Q}^- , so we define

$$\mathbf{Q}^G \equiv \|\mathbf{Q}^+, \mathbf{Q}^-\|. \quad (11)$$

The computation of the Godunov state makes it possible to use discontinuous approximations of the unknowns to solve accurately a physically continuous problem, such as the linear elastic wave equation. This is in fact the main ingredient of FV and DG methods. As an example, we can compute the Godunov state at a boundary for the one-dimensional boundary of length unity that connects two triangular cells. Figure 1 shows a polynomial representation of the shear stress σ_{xy} which is continuous inside each of the triangular domains but discontinuous at the interface. Assuming also a discontinuous state of the perpendicular velocity v , we can compute the Godunov state along the interface by applying the third and fifth equations in (10). The result is shown in Figure 1, where we have assumed $\rho = 1$, $\mu = 1$. The two interface values of the discontinuous variables produce one single Godunov state which is pointwise a linear combination of the values at both sides. As a consequence, the Godunov state is smooth if the values of the variables at both sides of the interface are smooth as well.

[13] In order to impose boundary conditions we must perturb the boundary variables out of their Godunov state. Obtaining the perturbed wave strengths in (6) and (8) that enforce a perturbed boundary variable is referred by *Käser and Dumbser* [2006] as solving the inverse Riemann problem. In our case, in order to impose a perturbed value of fault traction, $\tilde{\sigma}_{xy} = \sigma_{xy}^G + \delta\sigma_{xy}$, that satisfies a certain friction law, we need to apply

$$\underline{Q}_3(S^-) = \underline{Q}_3(S^+) = \tilde{\sigma}_{xy}. \quad (12)$$

We find that the perturbed values of the wave strengths that ensure (12) are

$$\begin{aligned} \alpha'_2 &= \alpha_2 + \frac{\delta\sigma_{xy}}{\mu}, \\ \alpha'_4 &= \alpha_4 - \frac{\delta\sigma_{xy}}{\mu}. \end{aligned} \quad (13)$$

Substituting these values into (6) and (8) leads to

$$\begin{aligned} \tilde{\underline{Q}}(S^+) &= \underline{Q}^G + \left(0, 0, \delta\sigma_{xy}, 0, \frac{c_s}{\mu} \delta\sigma_{xy}\right)^T, \\ \tilde{\underline{Q}}(S^-) &= \underline{Q}^G + \left(0, 0, \delta\sigma_{xy}, 0, -\frac{c_s}{\mu} \delta\sigma_{xy}\right)^T. \end{aligned} \quad (14)$$

Notice that (12) is fulfilled by (14) by design, but a side effect of the perturbation is that $\tilde{\underline{Q}}_5(S^+) \neq \tilde{\underline{Q}}_5(S^-)$, hence two different values for the boundary velocity are obtained:

$$\begin{aligned} \tilde{v}^+ &= v^G + \frac{c_s}{\mu} \left(\tilde{\sigma}_{xy} - \sigma_{xy}^G\right), \\ \tilde{v}^- &= v^G - \frac{c_s}{\mu} \left(\tilde{\sigma}_{xy} - \sigma_{xy}^G\right). \end{aligned} \quad (15)$$

Making use of the definitions of the Godunov variables σ_{xy}^G and v^G given in (10), we infer

$$\tilde{v}^+ = v^+ + \frac{c_s}{\mu} \left(\tilde{\sigma}_{xy} - \sigma_{xy}^+\right) \quad (16)$$

and

$$\tilde{v}^- = v^- - \frac{c_s}{\mu} \left(\tilde{\sigma}_{xy} - \sigma_{xy}^-\right). \quad (17)$$

These expressions are crucial for the understanding of fault dynamics using fluxes, as they state that a certain imposed traction value instantly and locally generates an imposed velocity parallel to the fault. Further, subtracting the equations in (15), we find the slip rate as

$$\Delta\tilde{v} = \frac{2c_s}{\mu} \left(\tilde{\sigma}_{xy} - \sigma_{xy}^G\right). \quad (18)$$

This shows that slip ($\Delta\tilde{v} \neq 0$) occurs only if $\tilde{\sigma}_{xy} \neq \sigma_{xy}^G$.

[14] Expression (18) is clearly different from the $\Delta v = v^+ - v^-$ commonly used in continuous methods such as FD or FE. Discontinuous methods as FV or DG display in general discontinuities between stresses and velocities at

any interface, but this does not represent a discontinuity of the physical variables themselves, which are uniquely determined by the Godunov state. The classical slip rate definition $\Delta v = v^+ - v^-$ is recovered if $\sigma_{xy}^+ = \sigma_{xy}^- = \tilde{\sigma}_{xy}$; that is, prescribing the traction states at both sides and at the interface to be identical. Only in this context do the classic and the discontinuous expressions for the slip rate fully agree.

[15] The rest of Godunov's variables, normal velocity and bulk stresses, can be all computed using (10) as they are independent of $\tilde{\sigma}_{xy}$, thus resulting in a physically continuous problem, although still with a discontinuous mathematical representation.

4. The Numerical Method

[16] In the ADER-DG approach a two-dimensional computational domain Ω is divided into conforming triangular elements $\mathcal{T}^{(m)}$ addressed by a unique index (m). The numerical solution of equation (4) is approximated inside each element $\mathcal{T}^{(m)}$ by a linear combination of space-dependent polynomial basis functions $\Phi_l(\xi)$ of degree N , where $\xi = (\xi, \eta)$ are the coordinates in a canonical reference element \mathcal{T}_E [Käser and Dumbser, 2006], and time-dependent degrees of freedom $\hat{Q}_{pl}^{(m)}(t)$

$$\underline{Q}_p^{(m)}(\xi, t) = \hat{Q}_{pl}^{(m)}(t)\Phi_l(\xi). \quad (19)$$

The index p is associated with the unknowns in the vector \underline{Q} . The index l indicates the l th basis function and ranges from 0 to $L - 1$, where $L = (N + 1)(N + 2)/2$ is the number of required basis functions in two dimensions for a polynomial degree N , leading to a numerical approximation of order $\mathcal{O} = N + 1$.

[17] Let us assume that the state of the variables \underline{Q}_p is known at a certain time level t . Then, multiplying (4) by a test function Φ_k and integrating over an element $\mathcal{T}^{(m)}$ and over a time interval of size Δt gives

$$\begin{aligned} &\int_t^{t+\Delta t} \int_{\mathcal{T}^{(m)}} \Phi_k \frac{\partial Q_p}{\partial t} dV dt \\ &+ \int_t^{t+\Delta t} \int_{\mathcal{T}^{(m)}} \Phi_k \left(A_{pq} \frac{\partial Q_q}{\partial x} + B_{pq} \frac{\partial Q_q}{\partial y} \right) dV dt = 0. \end{aligned} \quad (20)$$

Integration of equation (20) by parts yields

$$\begin{aligned} &\int_t^{t+\Delta t} \int_{\mathcal{T}^{(m)}} \Phi_k \frac{\partial Q_p}{\partial t} dV dt + \sum_{j=1}^3 \mathcal{F}_{pk}^j \\ &- \int_t^{t+\Delta t} \int_{\mathcal{T}^{(m)}} \left(\frac{\partial \Phi_k}{\partial x} A_{pq} + \frac{\partial \Phi_k}{\partial y} B_{pq} \right) Q_q dV dt = 0. \end{aligned} \quad (21)$$

Equation (21) can then be used to obtain the values of \underline{Q}_p at the following time level $t + \Delta t$, as explained in the introductory papers by Käser and Dumbser [2006] and Dumbser and Käser [2006]. In these seminal studies the

integration of the first and third terms in (21) are fully detailed. The second term is the sum of numerical fluxes \mathcal{F}_{pk}^j across the three edges, $j = 1, 2, 3$, of the triangular element, accounting for the possible discontinuity of \mathbf{Q} . Although its resolution for interfaces with no faults is described in the aforementioned papers, for the case of faults we require a different strategy, explained in section 4.1.

4.1. Fluxes at Faults

[18] We consider for simplicity a single edge of a triangular element with its normal aligned with the x axis and drop the j indices. The flux term in (21) can be expressed as

$$\mathcal{F}_{pk} = A_{pr} \int_t^{t+\Delta t} \int_S \Phi_k \tilde{Q}_r dS dt. \quad (22)$$

The integral covers the whole edge S and a time interval of size Δt . For standard interfaces without faults we have $\tilde{\mathbf{Q}} = \mathbf{Q}^G = \|\mathbf{Q}^+, \mathbf{Q}^-\|$, where \mathbf{Q}^G is the Godunov state created from the variable states \mathbf{Q}^+ and \mathbf{Q}^- at both sides of the fault. When faults are present, however, some of the values of $\tilde{\mathbf{Q}}$ must be imposed using, for example, the expressions derived in section 3 for LSW friction. In this particular case, for $Q_1 = \sigma_{xx}$, $Q_2 = \sigma_{yy}$ and $Q_4 = u$, expression (22) is exactly the same as that described in the flux formulation of *Käser and Dumbser* [2006]. In contrast, for $Q_3 = \sigma_{xy}$ and $Q_5 = v$ a different approach must be followed.

[19] A suitable temporal expansion of the variables at both sides is obtained via a Taylor expansion near the time instant t . At time $t + \tau$, with $\tau \leq \Delta t$, the expansion reads

$$Q_p(\boldsymbol{\xi}, t + \tau) = \sum_{k=0}^N \frac{\tau^k}{k!} \frac{\partial^k Q_p(\boldsymbol{\xi}, t)}{\partial t^k}. \quad (23)$$

The high-order time derivatives in (23) are substituted by spatial derivatives using the expression (4) in an iterative way

$$\frac{\partial^k Q_p(\boldsymbol{\xi}, t)}{\partial t^k} = (-1)^k \left(A_{pq} \frac{\partial}{\partial x} + B_{pq} \frac{\partial}{\partial y} \right)^k Q_q(\boldsymbol{\xi}, t). \quad (24)$$

This yields

$$Q_p(\boldsymbol{\xi}, t + \tau) = \sum_{k=0}^N \frac{\tau^k}{k!} (-1)^k \left(A_{pq} \frac{\partial}{\partial x} + B_{pq} \frac{\partial}{\partial y} \right)^k Q_q(\boldsymbol{\xi}, t). \quad (25)$$

The expansion (25) is performed separately for the unknown states $\mathbf{Q}^+(\boldsymbol{\xi}, t)$ and $\mathbf{Q}^-(\boldsymbol{\xi}, t)$ and then linearly combined according to (10) to obtain the temporal polynomial expansion of the Godunov state $\mathbf{Q}^G(\boldsymbol{\xi}, t) = \|\mathbf{Q}^+(\boldsymbol{\xi}, t), \mathbf{Q}^-(\boldsymbol{\xi}, t)\|$.

[20] In preparation for the numerical integration of the flux (22), we evaluate $\mathbf{Q}^G(\boldsymbol{\xi}, t)$ at a set of space-time Gaussian integration points along the triangle's edge at space locations $\boldsymbol{\xi}_i = (\xi_i, \eta_i)$, with $i = 1, \dots, 2N + 1$, and along the time axis at time levels $\tau_l \in [t, t + \Delta t]$, with $l = 1, \dots, N + 1$. We write

$$Q_{p,il}^G = Q_p^G(\boldsymbol{\xi}_i, \tau_l) = \hat{Q}_{ps}^G(\tau_l) \Phi_s(\boldsymbol{\xi}_i). \quad (26)$$

Notice that we are using more integration points than are sufficient for exact Gauss integration given the polynomial degree of the integrand in (22). Such large number of integration points can allow future, more general formulations where, for example, the material properties are variable inside one element.

[21] We solve for the fault physics locally, at each space-time integration point, in three steps. First, we evaluate the failure criterion (1) so that

$$\tilde{\sigma}_{xy,il} = \min \left\{ \sigma_{xy,il}^G, \mu_{f,il} \left(\sigma_{xx,il}^G + \sigma_{xx}^0 \right) - \sigma_{xy}^0 \right\}, \quad (27)$$

where $\mu_{f,il}$ is the local value of the dynamic friction coefficient and σ_{xx}^0 and σ_{xy}^0 are the initial normal and shear stress values, respectively. Once we have solved (27) for the point $(\boldsymbol{\xi}_i, \tau_l)$ we can compute the slip rate using (18) locally such that

$$\Delta \tilde{v}_{il} = \frac{2c_s}{\mu} \left(\tilde{\sigma}_{xy,il} - \sigma_{xy,il}^G \right). \quad (28)$$

The slip $\Delta \tilde{d}_{il}$ is obtained by integrating (28). Finally, we apply the LSW friction law (2) to obtain the time-updated value of $\mu_{f,il+1}$ as

$$\mu_{f,il+1} = \max \left\{ \mu_d, \mu_s - \frac{\mu_s - \mu_d}{D_c} \Delta \tilde{d}_{il} \right\}. \quad (29)$$

Equations (27), (28), and (29) are solved for each space-time integration point while ensuring causality by updating the time levels in a sequential way, i.e., from $l = 1$ to $l = N + 1$.

[22] The values of the velocities at each side of the fault can be retrieved from (16) and (17) as

$$\begin{aligned} \tilde{v}_{il}^+ &= v_{il}^+ + \frac{c_s}{\mu} \left(\tilde{\sigma}_{xy,il} - \sigma_{xy,il}^+ \right), \\ \tilde{v}_{il}^- &= v_{il}^- - \frac{c_s}{\mu} \left(\tilde{\sigma}_{xy,il} - \sigma_{xy,il}^- \right). \end{aligned} \quad (30)$$

Using the shear stress from (27) and the velocities from (27), all values of $\tilde{\mathbf{Q}}$ at the interface are then known and the flux (22) can be integrated numerically as

$$\mathcal{F}_{pk} = A_{pr} \sum_{i=1}^{2N+1} \sum_{l=1}^{N+1} \omega_i^S \omega_l^T \Phi_k(\boldsymbol{\xi}_i) \tilde{Q}_{r,il}. \quad (31)$$

where ω_i^S and ω_l^T are the weights of the spatial and temporal Gaussian integration, respectively. The appropriate value of the fault-parallel velocity, \tilde{v}^+ or \tilde{v}^- from equation (27), is employed depending on which side of the fault the element under consideration lies on.

[23] Although so far we have considered an edge that has its normal vector aligned with the x axis, we can generalize (31) to an arbitrary orientation of the normal vector \mathbf{n} as

$$\mathcal{F}_{pk} = T_{pq} A_{qr} \sum_{i=1}^{2N+1} \sum_{l=1}^{N+1} \omega_i^S \omega_l^T \Phi_k(\boldsymbol{\xi}_i) \tilde{q}_{r,il}, \quad (32)$$

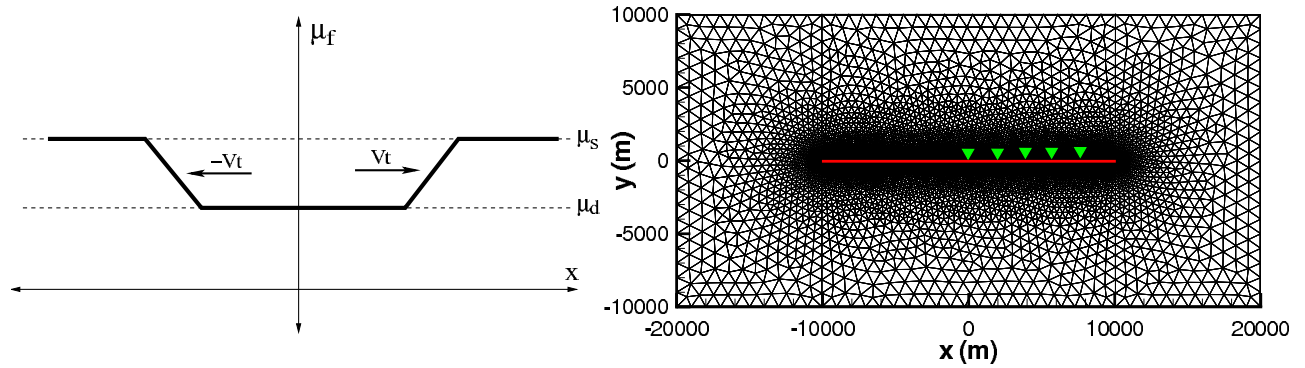


Figure 2. (left) Assumed friction along the fault in the self-similar crack case. The low-friction patch expands at constant velocity V . (right) Mesh used for this case. The red line depicts the fault and the triangles receiver locations.

where T is a rotation matrix, given explicitly by Käser and Dumbser [2006] and Dumbser and Käser [2006], and \tilde{q} are the variables transformed to the local edge coordinate system from the global xy -aligned one by

$$\tilde{q}_p = T_{pq}^{-1} \tilde{Q}_q. \quad (33)$$

The fault equations (27) to (27) are readily applied to \tilde{q} .

4.2. Stability Criterion

[24] In order to guarantee the numerical stability of our explicit time advancement scheme, we constrain the size of the time step following the Courant-Friedrichs-Lewy (CFL) criterion of Courant *et al.* [1928], thus having

$$\Delta t \leq \frac{C}{2N+1} \min\left(\frac{2r_{\text{in}}}{c_p}\right), \quad (34)$$

where C is an empirically determined constant (in the following we will use $C = 0.5$) and r_{in} is the radius of the in circle of the triangle. The minimum is taken among all elements in the domain. Note that this is the same stability criterion as that used for the ADER-DG method in the absence of faults.

5. Self-Similar Crack Validation Problem

[25] We test the performance of the ADER-DG scheme for the case of a self-similar crack. In this case the traction at the fault is imposed beforehand as a function of space and time, similarly to the case proposed by Kostrov [1964]. This problem and variations of it have been used in previous works on dynamic rupture modeling [e.g., Andrews, 1985; Cruz-Atienza and Virieux, 2004; Rojas *et al.*, 2008; Benjema *et al.*, 2007]. We remark that the problem is not really reproducing the dynamic behavior of a fault because the traction is imposed externally. However, in our case it is advantageous because it allows us to validate the relation between traction and slip rate (18) without having to solve any friction laws or failure criteria, which would add further errors in the final solutions. Furthermore it is easy to model it with the spectral boundary integral equation (SBIE) method in its BIMAT implementation [Cochard and Rice, 2000; Rubin and Ampuero, 2007]. The acknowledged accuracy of this last method makes it usable as a reference

solution for our purposes. In our case, the friction coefficient follows the expression

$$\mu_f(x, t) = \max\{\mu_d, \mu_s - (\mu_s - \mu_d)(Vt - |x|)/L\}, \quad (35)$$

where we choose to take the values $L = 250$ m, $V = 2000$ m/s, $\mu_s = 0.5$ and $\mu_d = 0.25$. The value of μ_f is depicted in Figure 2. The problem is further characterized by an initial normal stress of 40.0 MPa and shear stress of 20.0 MPa. We represent a straight fault 20 km long centered at the coordinates origin and surrounded by a homogeneous material with density $\rho = 2500$ kg/m³, P wave velocity $c_p = 4000$ m/s and S wave velocity $c_s = c_p/\sqrt{3}$, so the same material properties as those used by Benjema *et al.* [2007]. The simulation is performed on a rectangular domain of 40 km per 20 km, meshed with elements of 100 m edge length at the fault itself, as shown in Figure 2. The mesh is then smoothly coarsened toward the boundaries of the domain, thus having elements of a maximum of 1000 m edge length. In total the mesh contains 11850 elements. As a comparison, a regular triangular mesh containing equilateral triangles with resolution of 100 m everywhere would contain 13 times more elements. Figure 3 shows the solution obtained with a sixth-order ADER-DG scheme (ADER-DG $\mathcal{O}6$) recorded at five different receivers, separated 2000 m from each other, and compared to the reference solution. No large differences between the numerical and the reference solutions can be observed in the slip, slip rate or traction. Furthermore, we have plotted the root-mean-square (RMS) of the time histories of slip rate for the same receivers for the whole 5 s of simulation obtained with schemes $\mathcal{O}3$ to $\mathcal{O}6$. For distances 2000 m to 8000 m the high-order schemes produce both smaller errors and a slower decrease of accuracy at longer distances. At 2000 m, the schemes $\mathcal{O}4$ to $\mathcal{O}6$ produce roughly identical results. At longer distances the usage of the highest orders produces more precise results. It is worth noticing that no significant effects from the artificial absorbing boundaries or spurious oscillations are observed. We remark that no artificial damping has been used in any of the simulations.

6. Spontaneous Rupture Validation Problem

[26] We test the performance of the ADER-DG method on a 2-D version of the benchmark problem for spontaneous

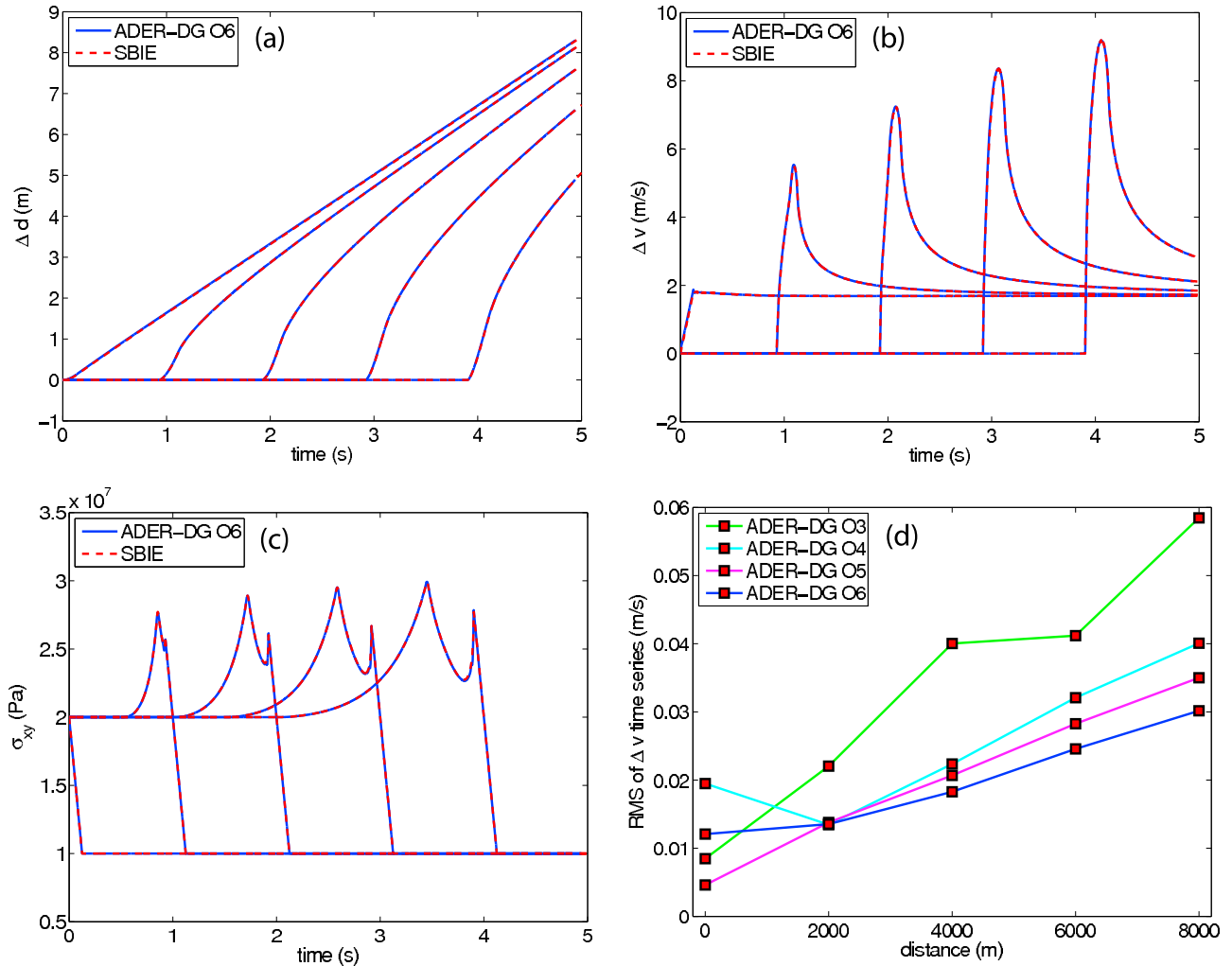


Figure 3. Results of the self-similar crack test obtained with the ADER-DG $\mathcal{O}6$ method (blue) and the SBIE method (red). (a) Slip, (b) slip rate, and (c) traction errors are measured on the fault at five points with hypocentral distance 0, 2, 4, 6 and 8 km. (d) RMS difference of the slip rate time histories as a function of hypocentral distance for orders $\mathcal{O}3$ to $\mathcal{O}6$.

rupture propagation of the Southern California Earthquake Center (SCEC). The original 3-D SCEC test (Version 3) is detailed by *Harris et al.* [2004]. The 2-D analog of this benchmark problem, considered here, was presented by *Rojas et al.* [2008] and used in further publications in order to assess the accuracy of numerical methods [e.g., *Kaneko et al.*, 2008]. The setup is a straight fault, represented by a 2-D line, embedded in a homogeneous elastic body. The fault is 30 km long, and the medium has a density of $\rho = 2670 \text{ kg/m}^3$, P wave velocity $c_p = 6000 \text{ m/s}$, and S wave velocity $c_s = 3464 \text{ m/s}$. A nucleation zone of 3 km is defined at the center of the fault. The fault is governed by a LSW friction law with the parameters given in Table 1.

[27] The problem has been tested in eight different meshes, comprising computational domains of size $72 \times 72 \text{ km}$, with edge lengths h ranging from 100 m to 1500 m. All meshes are completely unstructured, with regular mesh spacing forced along the fault plane. The mesh is gradually coarsened toward the external boundaries, up to an edge spacing 10 times larger than that at the fault. We have employed different orders, from $\mathcal{O}2$ to $\mathcal{O}6$. The equivalent

mesh spacing, accounting for the polynomial subcell resolution, is $\Delta x = h/(N + 1)$.

6.1. Comparison to Other Methods

[28] We first study the similarities between existing numerical methods and the ADER-DG method developed here. We solved the 2-D analog of the SCEC test problem with the following methods: (1) the ADER-DG $\mathcal{O}6$ method using an edge length $h = 150 \text{ m}$, which leads to an equivalent mesh spacing of $\Delta x = 25 \text{ m}$, (2) the spectral boundary integral equation (SBIE) method of *Geubelle and*

Table 1. Parameters Describing the Fault for the SCEC Test Case

| Parameter | Nucleation Zone | Outside Nucleation Zone |
|-------------------------------|-----------------|-------------------------|
| Initial shear traction (MPa) | 81.6 | 70.0 |
| Initial normal traction (MPa) | 120.0 | 120.0 |
| Static friction coefficient | 0.677 | 0.677 |
| Dynamic friction coefficient | 0.525 | 0.525 |
| Critical slip distance (m) | 0.4 | 0.4 |

Rice [1995] in the multidimensional spectral boundary integral (MDSBI) implementation (E. Dunham, MDSBI: Multidimensional spectral boundary integral, version 3.9.10, 2008, available at <http://pangea.stanford.edu/~edunham/codes/codes.html>) and a node spacing of $\Delta x = 12.5$ m, (3) the traction-at-split-node (TSN) FD method described by Andrews [1973], (4) the staggered-grid split node (SGSN) FD method developed by Dalguer and Day [2007], in particular, the 2-D second-order implementation of Brietzke et al. [2009]. Both FD methods use similar representations of the fault zone and a node spacing of $\Delta x = 12.5$ m with no artificial damping, (5) the spectral element (SE) method (J.-P. Ampuero, SEM2DPACK: A spectral element method for 2-D wave propagation and earthquake source dynamics, version 2.3.3, 2008, available at <http://sourceforge.net/projects/sem2d/>), with a much finer resolution $\Delta x = 6.25$ m and with no artificial damping, and (6) the same SE method but with Kelvin-Voigt damping (SE-KV) as described by Day and Ely [2002], restricted here to a two-element wide layer around the fault, with artificial viscosity $\gamma = 0.1\Delta t$.

[29] Figure 4 shows slip rate and shear stress for all methods on the fault point located at $x = 12.5$ km. All computed solutions agree in their main features. A first issue apparent from the slip rate plots in Figures 4a and 4b is that both FD and SE undamped simulations produce high-frequency oscillations of amplitudes around 3% of the peak slip rate value. These oscillations are strongly reduced by adding artificial damping terms to the governing equations, as illustrated in Figure 4c by the SE-KV simulation, although the oscillations do not vanish completely with our choice of γ . Increasing further the artificial viscosity can eliminate the oscillations but has also negative side effects such as a decrease in the peak slip rate and a delay in the rupture times [see, e.g., Dalguer and Day, 2007]. The ADER-DG solutions are remarkably smooth, similar to SBIE solutions, despite containing no additional damping. In fact, the ADER-DG and the SBIE solutions in Figures 4b and 4e are virtually identical, except for a small oscillation of frequency around 30 Hz.

[30] To further explore the frequency dependence of all solutions, we plot in Figure 5 the slip rate spectra, evaluated over a Gaussian-tapered time window containing the rupture front but not the healing fronts, thus avoiding further high-frequency contributions not coming from the rupture front itself. Good agreement between all methods is obtained at low and intermediate frequencies, up to 20 or 30 Hz. Moreover, the spectral decay exponents are consistent with theoretical expectations. Recall that if slip rate behaves as t^α , where t is time after the rupture front, then its spectrum behaves as $f^{-1-\alpha}$. At low frequencies (below 10 Hz in this example) slip rate spectra decay as $f^{-1/2}$, consistent with the $1/\sqrt{t}$ behavior of singular crack models. At intermediate frequencies (above 10 Hz in this example) the $f^{-3/2}$ decay is consistent with the \sqrt{t} onset predicted analytically for slip-weakening crack models under the assumption of a steady state process zone [Ida, 1973]. At very high frequencies the FD and SE methods develop numerical artifacts due to the dispersion relation of the discrete lattice. Artificial damping reduces significantly the amplitude of these artifacts. Comparing the undamped and damped SE simulations reveals that numerical artifacts

(spectral peaks) are excited beyond 100 Hz in this example. In contrast, the ADER-DG results have a smooth spectral decay without sign of spuriously amplified modes.

6.2. Convergence of the ADER-DG Method

[31] Since analytical solutions do not exist for the spontaneous rupture problem, one cannot determine with absolute certainty which numerical solutions solve the proposed test better. We measure the error of the ADER-DG method by the RMS difference of rupture time, peak slip rate and final slip between our finest grid solution ($\mathcal{O}6$, 100 m edge length) and the solutions for coarser grids. This particular error norm choice will further allow us to compare the accuracy of our method with other numerical solutions. For a justification of the usage of fine-grid solutions for convergence analysis we refer the reader to the appendix of Goto and Bielak [2008]. The RMS are evaluated on fault points spaced every 62.5 m from the nucleation point, and are expressed as a percentage of the RMS value along the whole fault obtained with our finest solution. The RMS values for the rupture time, peak slip rate and final slip are 2.92 s, 6.78 m/s and 5.90 m, respectively. Receivers located at vertices of triangles are ignored, as they show unrepresentative errors due to the undefined Riemann problem solution at points that are common to more than two elements. The amount of points involved in the RMS computation range from 144 to 207. The difference in rupture time is measured as the first time sample at which the slip rate exceeds the value of 1 mm/s. The peak slip rate value has been obtained by finding the maximum of an interpolating cubic polynomial around the maximum of the slip rate time histories.

[32] The results of the simulations are compiled in Table 2 and plotted in Figure 6. We observe that lower-order schemes can only achieve equivalent errors as higher-order schemes when using a smaller equivalent mesh spacing. Similarly, a better accuracy is obtained for higher-order schemes for the same equivalent node spacing. From Figure 6a it is clear that, when reaching rupture time difference values close to Δt , the accuracy of all solutions collapse to values on the order of the transit time of the rupture front across a nodal spacing Δx , which is proportional to Δt , as has been previously observed for other numerical methods [Day et al., 2005; Dalguer and Day, 2007]. Considering only simulations with RMS above this $\propto \Delta t$ asymptote, the rupture time differences as a function of average grid size Δx behave as a power law with convergence exponents (the slopes of the log-log convergence plots) ranging from 1.54 to 2.26, as shown in Table 3. On the other hand, taking only those points obtained with $\mathcal{O}6$ simulations which lie at Δt accuracy we obtain a slope of 1.15, similar to the theoretical power law exponent 1 followed by the time step, as in general the time step (34) is linearly proportional to the minimum mesh spacing. For all cases the scattering around the least squares values is noticeable, due to the use of completely unstructured meshes.

[33] An indicator of the resolution required to model the rupture process with sufficient accuracy is the number of points per median cohesive zone size, $\bar{N}_c = \bar{\Lambda}/\Delta x$. The value of the median cohesive zone size $\bar{\Lambda} = 258$ m was obtained by Rojas et al. [2008] for the 2-D analog of the SCEC test. Figure 6a shows that ADER-DG $\mathcal{O}6$ yields RMS errors in

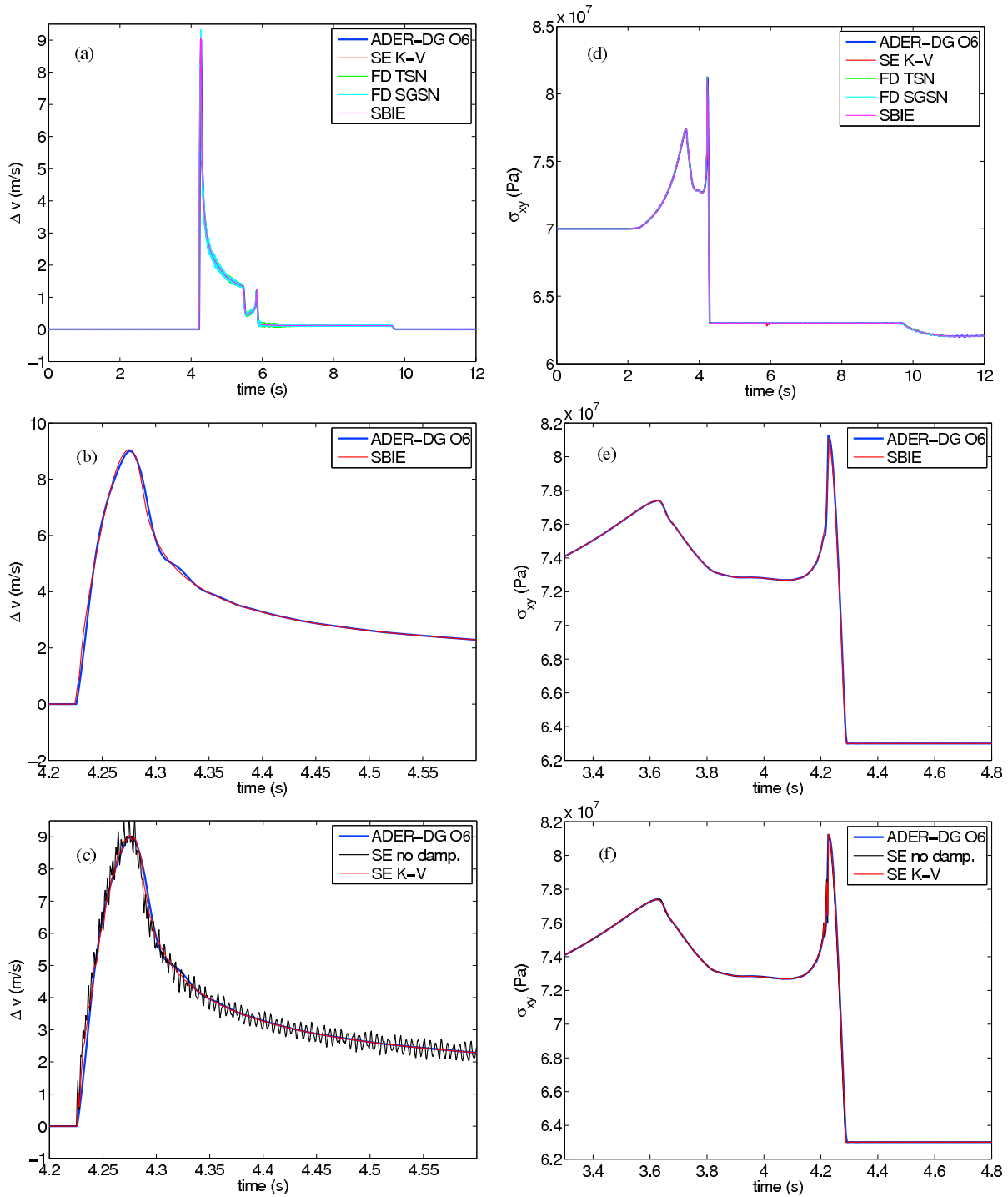


Figure 4. (a) Slip rate and (d) traction recorded at a receiver situated at $x = 12.5$ km. One SE, two FD, and a SBIE implementations are compared to the ADER-DG solution. Zoom of (b) the slip rate and (e) traction for SBIE close to the rupture front. (c) Slip rate and (f) traction compared to the SE method solution with and without Kelvin-Voigt damping.

rupture times below 0.3% with $\overline{N_c} \approx 1.5$, corresponding to a mesh spacing $h \approx 1000$ m. This performance is superior to that of the mimetic operator split node (MOSN) scheme and the DFM studied by *Rojas et al.* [2008], which achieved 0.3% RMS rupture time error at $\overline{N_c} \approx 3.2$ and $\overline{N_c} \approx 4.3$, respectively. We note though that these convergence studies

must be compared with caution because their respective error norms are based on different reference solutions.

[34] The computational time was measured in all simulations, performed on a single Pentium 4 2.8 GHz processor. Figure 6b shows cost efficiency curves for the ADER-DG method of different orders, defined as the computational

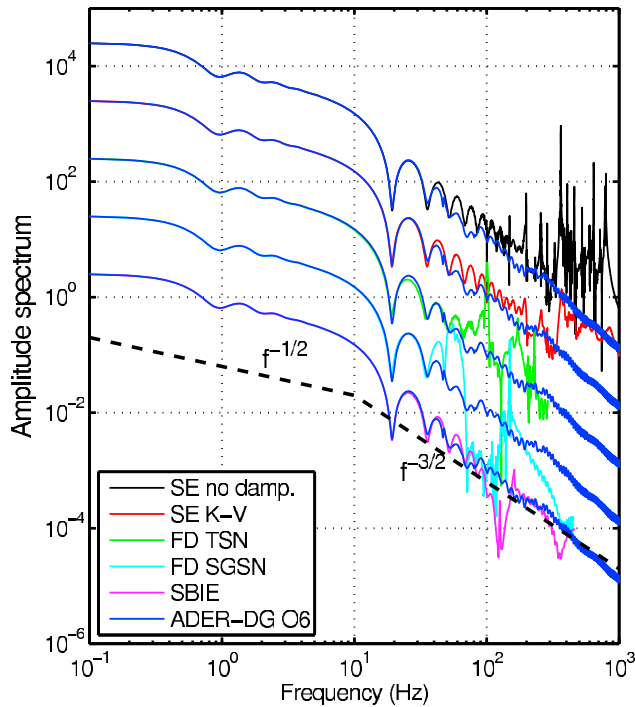


Figure 5. Spectra of the a window of slip rate at $x = 12.5$ km tapered near the rupture front for the SCEC test problem solved with several methods. Dashed lines indicate theoretical expectations, $f^{-1/2}$ at frequencies lower than 10 Hz and $f^{-3/2}$ at higher frequencies. The SBIE line has the correct offset, whereas all others have been shifted by a factor 10 in amplitude.

time required to achieve a given accuracy. The schemes of orders $\mathcal{O}4$ to $\mathcal{O}6$ have a similar efficiency which is superior to orders $\mathcal{O}2$ and $\mathcal{O}3$, for coarser meshes. After the Δt limit is reached, the trade-off rate drops to a smaller value.

[35] The final slip error, shown in Figure 6c, has a behavior similar to the rupture time error, although with smaller convergence exponents ranging from 0.87 to 1.27, as shown in Table 3. The RMS slip error is however not representative of the whole fault: the maximum slip misfits accumulate on elements containing the fault tips. The fraction of the total RMS accumulated on fault tip elements is higher than 60% in all but three simulations of order higher than $\mathcal{O}2$, averaging a value of 70.8% through all simulations performed. These errors most likely reflect problems capturing sudden, and probably unrealistic, rupture stopping conditions and can be reduced by smoother transitions to larger strength excess or larger fracture energy. These errors do not visibly propagate across the fault, as the stopping phases are accurately captured in our slip rate time histories elsewhere (see, e.g., Figure 4a). The errors in slip ignoring the fault tip elements are around two thirds of the values shown in Figure 6c.

[36] The peak slip rate differences are plotted in Figure 6d. For the coarser Δx values, the order of the ADER-DG scheme has little impact on the peak slip error. However, for resolutions finer than $\Delta x = 100$ m the different convergence exponents produce significant differences in

the RMS obtained with different schemes for the same spatial sampling.

7. Mesh Coarsening and Absorbing Boundaries

[37] Throughout sections 4 and 5 we have used meshes with high ratios of coarsening toward the exterior domain boundaries. No strong reflecting phase appears to affect our results on the fault. However we wish to explore the effect of the coarsening on the propagating waves generated by the fault rupture.

[38] We record the fault-parallel velocity, u , at 35 receivers located at coordinates $(0, i)$ km with $i = 1, \dots, 35$. We perform two new simulations with an $\mathcal{O}4$ scheme, using a mesh spacing at the fault of $h = 375$ m, which corresponds to $\Delta x = 93.75$ m. The first simulation is performed in the coarsened mesh used in section 6, with 5862 elements of size up to $h = 3750$ m. The second simulation uses a uniform mesh with constant element size $h = 375$ m, with 83,220 elements, roughly 14 times more elements than in the coarsened mesh.

Table 2. Results of the Simulations Realized for the SCEC Test

| h (m) | \mathcal{O} | Δx (m) | RMS Rupture Time (%) | RMS Final Slip (%) | RMS Peak Slip Rate (%) | CPU (s) |
|---------|---------------|----------------|-----------------------|-----------------------|------------------------|---------|
| 1500 | 4 | 375 | 2.20×10^0 | 2.85×10^0 | 4.11×10^1 | 68 |
| | 5 | 300 | 1.16×10^0 | 1.88×10^0 | 3.52×10^1 | 122 |
| | 6 | 250 | 5.97×10^{-1} | 1.30×10^0 | 3.00×10^1 | 216 |
| 750 | 2 | 375 | 4.81×10^0 | 7.95×10^0 | 5.06×10^1 | 74 |
| | 3 | 250 | 2.11×10^0 | 2.15×10^0 | 3.82×10^1 | 133 |
| | 4 | 187.5 | 6.09×10^{-1} | 1.23×10^0 | 2.74×10^1 | 286 |
| 500 | 5 | 150 | 2.30×10^{-1} | 7.74×10^{-1} | 2.10×10^1 | 589 |
| | 6 | 125 | 1.25×10^{-1} | 5.25×10^{-1} | 1.51×10^1 | 1,051 |
| | 2 | 250 | 2.04×10^0 | 6.12×10^0 | 4.56×10^1 | 129 |
| 375 | 3 | 166.6 | 6.14×10^{-1} | 1.52×10^0 | 3.06×10^1 | 272 |
| | 4 | 125 | 1.86×10^{-1} | 8.73×10^{-1} | 1.98×10^1 | 535 |
| | 5 | 100 | 1.03×10^{-1} | 5.48×10^{-1} | 1.29×10^1 | 1,080 |
| 300 | 6 | 83.3 | 8.46×10^{-2} | 3.70×10^{-1} | 7.55×10^0 | 2,082 |
| | 2 | 187.5 | 1.39×10^0 | 4.42×10^0 | 4.12×10^1 | 388 |
| | 3 | 125 | 3.63×10^{-1} | 1.15×10^0 | 2.35×10^1 | 805 |
| 250 | 4 | 93.7 | 1.11×10^{-1} | 6.40×10^{-1} | 1.25×10^1 | 1,561 |
| | 5 | 75 | 8.10×10^{-2} | 3.91×10^{-1} | 6.99×10^0 | 3,056 |
| | 6 | 62.5 | 5.88×10^{-2} | 2.52×10^{-1} | 3.75×10^0 | 6,021 |
| 187.5 | 2 | 150 | 1.24×10^0 | 3.62×10^0 | 3.58×10^1 | 538 |
| | 3 | 100 | 2.49×10^{-1} | 8.39×10^{-1} | 1.90×10^1 | 1,298 |
| | 4 | 75 | 8.60×10^{-2} | 4.78×10^{-1} | 9.41×10^0 | 2,685 |
| 150 | 5 | 60 | 6.11×10^{-2} | 2.89×10^{-1} | 4.45×10^0 | 5,669 |
| | 6 | 50 | 4.47×10^{-2} | 1.72×10^{-1} | 2.65×10^0 | 11,822 |
| | 2 | 125 | 7.83×10^{-1} | 2.59×10^0 | 3.38×10^1 | 821 |
| 100 | 3 | 83.3 | 1.41×10^{-1} | 7.87×10^{-1} | 1.68×10^1 | 1,851 |
| | 4 | 62.5 | 6.27×10^{-2} | 4.18×10^{-1} | 6.80×10^0 | 4,116 |
| | 5 | 50 | 6.51×10^{-2} | 2.33×10^{-1} | 3.24×10^0 | 8,432 |
| 75 | 6 | 41.7 | 3.87×10^{-2} | 1.89×10^{-1} | 2.33×10^0 | 17,296 |
| | 2 | 93.5 | 6.57×10^{-1} | 1.96×10^0 | 2.57×10^1 | 1,287 |
| | 3 | 62.3 | 1.40×10^{-1} | 5.89×10^{-1} | 9.20×10^0 | 3,072 |
| 50 | 4 | 46.7 | 8.12×10^{-2} | 2.82×10^{-1} | 3.72×10^0 | 6,638 |
| | 5 | 37.4 | 5.48×10^{-2} | 1.79×10^{-1} | 3.62×10^0 | 14,078 |
| | 6 | 31.7 | 3.66×10^{-2} | 1.41×10^{-1} | 2.21×10^0 | 28,110 |
| 30 | 2 | 75 | 3.84×10^{-1} | 1.97×10^0 | 2.30×10^1 | 1,948 |
| | 3 | 50 | 7.89×10^{-2} | 5.05×10^{-1} | 8.31×10^0 | 4,067 |
| | 4 | 37.5 | 3.96×10^{-2} | 3.15×10^{-1} | 2.68×10^0 | 8,249 |
| 20 | 5 | 30 | 2.79×10^{-2} | 9.23×10^{-2} | 2.23×10^0 | 16,604 |
| | 6 | 25 | 1.70×10^{-2} | 6.32×10^{-2} | 1.33×10^0 | 33,110 |
| | 2 | 50 | 1.75×10^{-1} | 1.58×10^0 | 1.67×10^1 | 4,598 |
| 16.7 | 3 | 33.3 | 3.79×10^{-2} | 2.79×10^{-1} | 3.98×10^0 | 9,596 |
| | 4 | 25 | 1.81×10^{-2} | 1.27×10^{-1} | 1.98×10^0 | 19,578 |
| | 5 | 20 | 7.07×10^{-3} | 5.54×10^{-2} | 5.50×10^{-1} | 39,593 |
| 6 | 16.7 | 0 | 0 | 0 | 80,000 | |

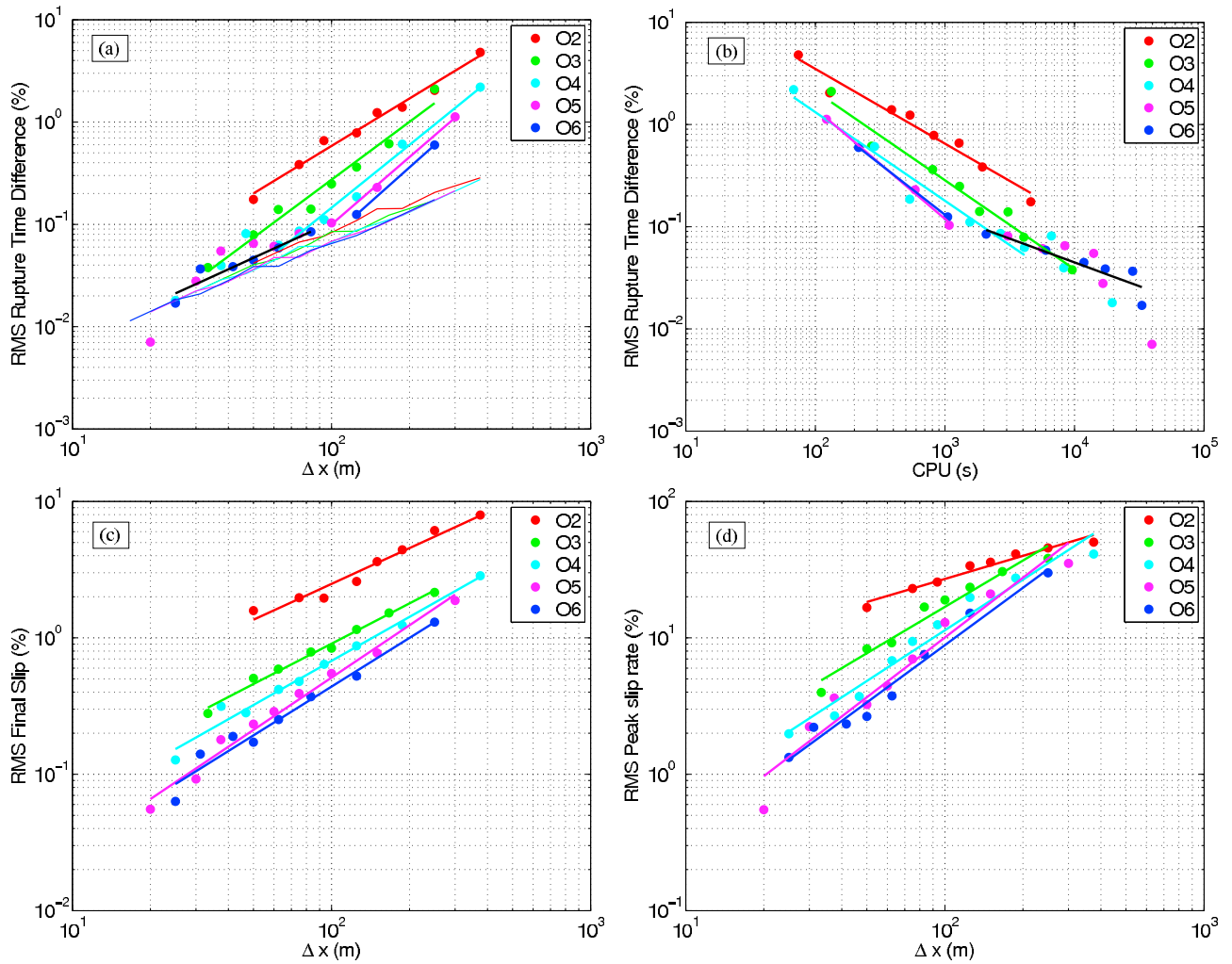


Figure 6. Convergence results for the 2-D analog SCEC test. Dots are simulation results. Colored thick lines of different steep slopes show least squares fits of these dots obtained by different orders of accuracy. To this end, we used only dots which have not reached the Δt uncertainty levels, whereas the thick black line has been obtained by fitting the remaining points. The thin lines of smaller slope represent the uncertainty levels determined by the Δt values. Misfits are shown for (a) rupture time, (c) final slip, and (d) peak slip rate. (c) The convergence of the rupture time misfit as a function of its computational cost.

[39] The results obtained with both meshes, plotted in Figure 7, show two clear behaviors. First, no main reflection phase is observed in any of the seismograms. This is to be expected because, on the receiver line, the main reflected energy has normal incidence to our absorbing boundaries (see Käser and Dumbser [2006] for details on the absorbing boundary condition) which have a much better performance for this case than for incidence at grazing angles. In addition, we observe that the seismograms lose high-frequency content as we move away from the fault toward larger elements.

[40] To quantify the latter effect, we study some receivers situated at elements of known size and analyze their velocity amplitude spectra (Figure 8). The low frequencies are identical for both meshes. The high frequencies begin to differ from a certain corner frequency which becomes lower as the size of the elements increases. This frequency is

found to be approximately $f_m = 0.69c_s/h$ Hz in the present case. Figure 8 shows seismograms obtained with the coarsened mesh, unfiltered, and seismograms obtained with the uniform mesh, low-pass filtered with corner frequencies $f_m^{h=500} = 5$ Hz, $f_m^{h=1000} = 2.5$ Hz and $f_m^{h=1300} = 1.9$ Hz. The minimum wavelength resolvable with our scheme is $\lambda_{\min} = 1.45h$, so that we can resolve wavelengths down to approximately 1.45 times the size of our elements.

Table 3. Error Convergence Exponents for Schemes of Different Order

| Error Metric | O2 | O3 | O4 | O5 | O6 |
|----------------|------|------|------|------|------|
| Rupture time | 1.54 | 1.88 | 2.04 | 2.19 | 2.26 |
| Final slip | 0.87 | 0.98 | 1.07 | 1.27 | 1.19 |
| Peak slip rate | 0.56 | 1.13 | 1.23 | 1.45 | 1.40 |

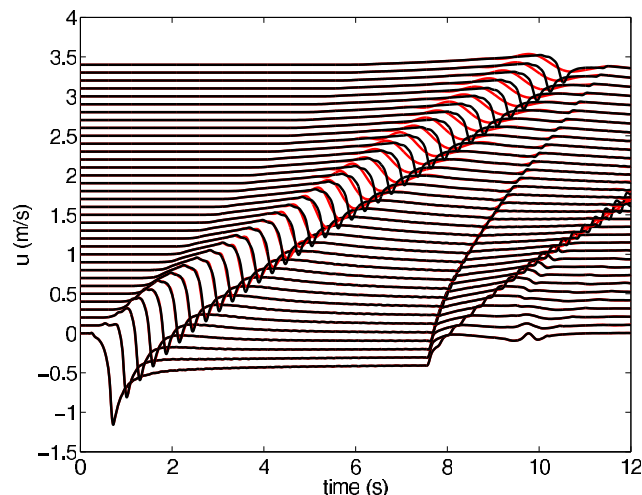


Figure 7. Fault-parallel velocity seismograms registered with 1 km spacing from the hypocenter, along the $x = 0$ axis, obtained with (black) a homogeneous mesh and (red) a graded mesh with a factor 10 coarsening toward the domain boundaries.

For a more thorough study on numerical accuracy of the ADER-DG scheme related to mesh size and propagated wavelengths, see Käser *et al.* [2008].

8. Dynamic Rupture on a Branched Fault System

[41] To show the potential of unstructured triangular meshes to represent complex fault systems, we simulate an earthquake occurring on the fault system that ruptured during the 28 June 1992 Landers earthquake ($M_w = 7.3$). This earthquake has been previously studied through 3-D dynamic rupture modeling using the boundary integral equation (BIE) method [Aochi and Fukuyama, 2002; Aochi *et al.*, 2002]. The fault system consists of six subfaults. The hypocenter is situated on its southernmost segment, the Johnson Valley fault, at a point which is the coordinate origin of our model.

[42] We assume a homogeneous initial stress field with principal stresses $\sigma_1 = 300$ MPa and $\sigma_3 = 100$ MPa and principal direction N22°E. This creates a heterogeneous stress state along the fault due to the orientation of the strike relative to the principal stresses. The fault has the homogeneous frictional parameters given in Table 4. The nucleation is forced by imposing a lower principal stress value of $\sigma_3 = 70$ MPa over a radius of 1.5 km around the hypocenter. The fault is allowed to rupture spontaneously for 10 s.

[43] We have used a circular domain of 120 km radius, using a mesh spacing of $h = 600$ m at the fault and coarsened up to $h = 6$ km for a total of 9605 elements. The mesh details can be seen in Figure 9. The simulation has been performed using an ADER-DG $\mathcal{O}5$ scheme, reaching the desired simulation time in 2.3 h in a single Pentium 4 2.8 GHz processor.

[44] Figure 10 shows snapshots of particle velocity generated by the earthquake. The rupture initially propa-

gates bilaterally (Figure 10a). After approximately 2 s the northern rupture front faces the choice of following the Johnson Valley fault or breaking the eastern Kickapoo fault (Figure 10b). This second option seems to be favored as the energy concentrates on the eastern side of the Kickapoo fault. Later on the rupture propagates all along the Kickapoo fault and extends to the Homestead Valley fault. The rupture reaches a relatively sudden end at a kink situated approximately at $(-2, 17)$ km and radiates a circular wavefront (Figure 10c). After 6 s most of the rupture has already stopped (Figure 10d).

[45] Aochi *et al.* [2002] showed that using a homogeneous initial stress the Kickapoo fault does not break, and rupture is confined to the Johnson Valley fault. In order to successfully reproduce the rupture pattern of the Landers earthquake, the authors used heterogeneous initial stress fields. In our 2-D simulation, in order to keep the setup as simple as possible, we kept the initial stress field homogeneous. However, this requires a large nucleation strength excess to break the Kickapoo and Homestead Valley faults, and produces unrealistically large slip at the Johnson Valley fault, of up to 12.3 m. Moreover, the northern branch of the Johnson Valley fault breaks with slip values of around 4 m, compared to the up to 6 m of slip recorded at the Kickapoo fault, and certain locations of the northernmost segments also break eventually with final slip values of up to 1 m in very small patches. These differences between our 2-D results and previous 3-D results are expected, and the only purpose of this exercise is to illustrate the potential of our new method.

9. Discussion

[46] The convergence test quantifies the accuracy of the ADER-DG method for the 2-D analog of the SCEC benchmark problem. To put these results in context, we compare them to the performance of the following four methods for the same problem: an FV method developed by Benjema *et al.* [2007], the SE method described by Kaneko *et al.* [2008], and two FD implementations (MOSN and DFM) presented by Rojas *et al.* [2008]. For the first two methods there is published information only on rupture time errors, whereas for the other two there is also information on peak slip rate and final slip errors. For each method, the reported errors are relative to the highest resolution simulation computed with that given method. Two attributes are summarized in Table 5: the convergence order before Δt saturation and the error obtained with average grid spacing $\Delta x = 100$ m.

[47] The second attribute has some bias due to the use of different reference solutions for each method. Whereas Rojas *et al.* [2008] noted that convergence rates and misfit at $\Delta x = 100$ m for the original 3-D version of the SCEC problem are systematically better than for the 2-D version, we expect the overall differences in accuracy between methods to be independent of the dimensionality of the problem.

[48] In terms of rupture time, ADER-DG $\mathcal{O}6$ compares favorably to all other 2-D methods studied. In terms of final slip DFM has better convergence rate than both ADER-DG and MOSN, but ADER-DG has lower error at $\Delta x = 100$ m. For peak slip rates the situation reverts: ADER-DG shows a

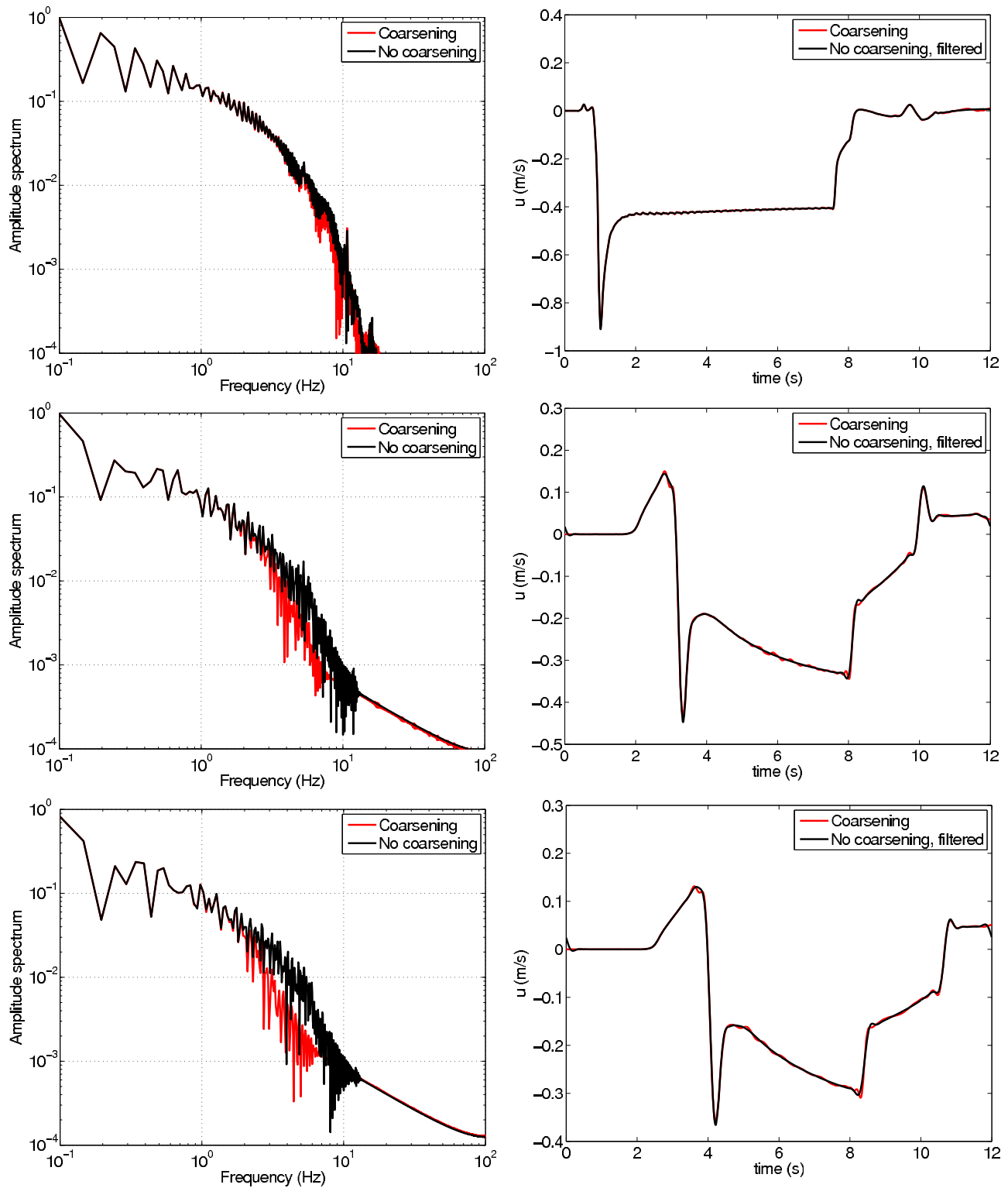


Figure 8. (left) Amplitude spectra for the uniform (black) and the coarsened mesh (red), for receivers situated at 2, 10, and 13 km, respectively. For the coarse mesh this corresponds to element sizes of 500, 750, and 1300 m, respectively. (right) Seismograms obtained with the coarsened mesh (red) and uniform mesh (black), low-passed filtered below 5, 2.5, and 1.9 Hz, respectively.

better convergence rate whereas both MOSN and DFM are more accurate at $\Delta x = 100$ m. Overall, ADER-DG yields results of similar or better accuracy than other existing methods for the 2-D analog of the SCEC test.

[49] The most remarkable outcome of the code comparison exercise in section 6.1 is the relative smoothness of the ADER-DG solution, which is free of spurious high-frequency oscillations. One possible reason for this feature

Table 4. Frictional Parameters for the Landers Fault System

| Parameter | Nucleation Zone | Outside Nucleation Zone |
|-----------------------------------|-----------------|-------------------------|
| Principal stress σ_1 (MPa) | 300.0 | 300.0 |
| Principal stress σ_3 (MPa) | 70.0 | 100.0 |
| Static friction coefficient | 0.6 | 0.6 |
| Dynamic friction coefficient | 0.4 | 0.4 |
| Critical slip distance (m) | 0.8 | 0.8 |

is that ADER-DG captures the analytical form of the fault stress response at very high frequencies. In fact, (18) can be rewritten as

$$\tilde{\sigma}_{xy} = \frac{\mu}{2c_s} \Delta \tilde{v} + \sigma_{xy}^G. \quad (36)$$

This is analogous to the analytical formulation of the problem as a boundary integral equation problem, the basis of the BI method [e.g., *Cochard and Madariaga, 1994*], in which the fault tractions are expressed as the sum of a radiation damping term ($\mu\Delta v/2c_s$) and tractions induced by the previous slip history. The radiation damping term is the instantaneous (high frequency) response of the fault stress to slip rate fluctuations. In contrast, FD, FE and SE methods implemented with the natural TSN approach lead to a discrete equation of the form

$$\sigma_{xy} = M\Delta a + \sigma_{xy}^t. \quad (37)$$

where M is an effective mass, Δa is slip acceleration and σ_{xy}^t is a trial stress evaluated from previous values under the assumption of no further slip [see, e.g., *Andrews, 1999*, equation 3]. We refer here to a primordial relation between traction and slip that depends on the spatial discretization but not on the time discretization scheme. At high frequencies the fault stress fluctuations in both equations (36) and (37) are dominated by the first term of their right hand side, the second term fluctuates more slowly. In FD, FE and SE the second-order, inertial term of equation (37) naturally leads to oscillatory behavior, whereas in ADER-DG and BI the first-order nature of this term in equation (36) leads to the expected radiation-damped behavior.

[50] The practical implication of the absence of amplification of spurious modes is that ADER-DG simulations do not require artificial handling of high frequencies, such as artificial viscous damping or postprocessing filtering. Spurious oscillations pose no serious problem for linear systems, as they can be eliminated by low-pass filtering in a postprocessing stage without compromising the low frequencies. However, for strongly nonlinear problems the spurious oscillations can lead to instabilities or inaccurate results, and are typically damped by artificial viscous terms, like the Kelvin-Voigt mechanism described by *Day and Ely [2002]*. Artificial viscosity introduces additional dissipation that can affect the solution; for instance, it tends to reduce the rupture speed. Not requiring artificial viscosity in ADER-DG clearly poses a benefit in terms of not introducing accuracy losses due to additional dissipation. Moreover, a proper control on numerical dissipation is particularly important in ill-posed dynamic rupture problems that require regularization, for instance, in some bimaterial rupture

problems [e.g., *Cochard and Rice, 2000*]. As the nonlinearities in dynamic rupture problems are strictly related to the choice of the friction law, one might expect instabilities to show up more strongly for certain laws. In LSW simulations the oscillations do not lead to propagating instabilities, but a stronger feedback would be expected with velocity-dependent friction laws. Fortunately, usual regularizations of velocity-weakening friction by a state variable reduce the order of the rupture front singularity and the amplitude of the associated spurious oscillations, which in practice yields accurate results without artificial damping [*Kaneko et al., 2008*].

[51] Some aspects of the current formulation of the ADER-DG method for dynamic rupture can be further improved. The first and perhaps more obvious is the linearization approximation assumed when adopting expression (25). Basically, for the time sub levels between two time steps we use predictions of the elastic unknowns obtained with continuous elastic theory, i.e., without faults, based on the so-called Cauchy-Kovalevski procedure [*Käser and Dumbser, 2006*]. This is clearly inappropriate and a correct study should use a Taylor expansion of the variables which already includes the rupture criterion (27) to recover better convergence rates, for example following what is shown by *Castro and Toro [2008]* for other nonlinear systems. Nevertheless, using the linearized version of the problem is already producing results which we consider satisfactory.

[52] The ADER-DG scheme, for linear seismic wave propagation problems, is a relatively expensive method in terms of computing time required per element. The addition of fault dynamics in the simulations has little impact on its performance. For the 2-D analog of the SCEC test case, we observe an increase of the CPU time of about 4.5% in the worst case with respect to a simulation on the continuous elastic case with the same mesh and with an identical order and number of iterations. We regard this percentage as negligible.

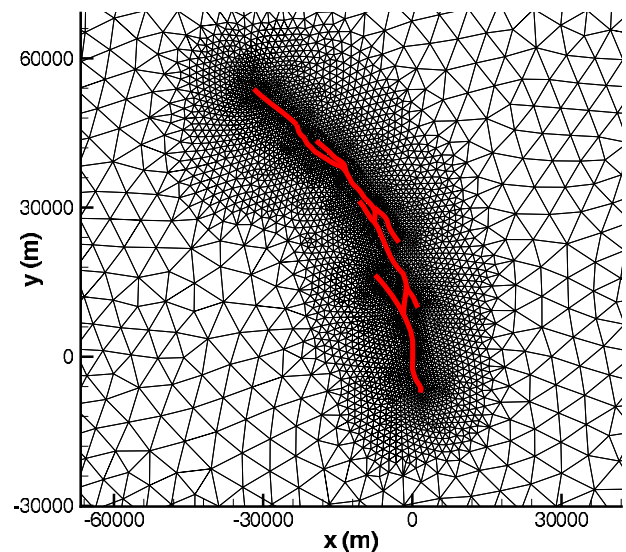


Figure 9. Mesh used for simulation of the dynamic rupture of the Landers fault system. The red line depicts the fault traces.

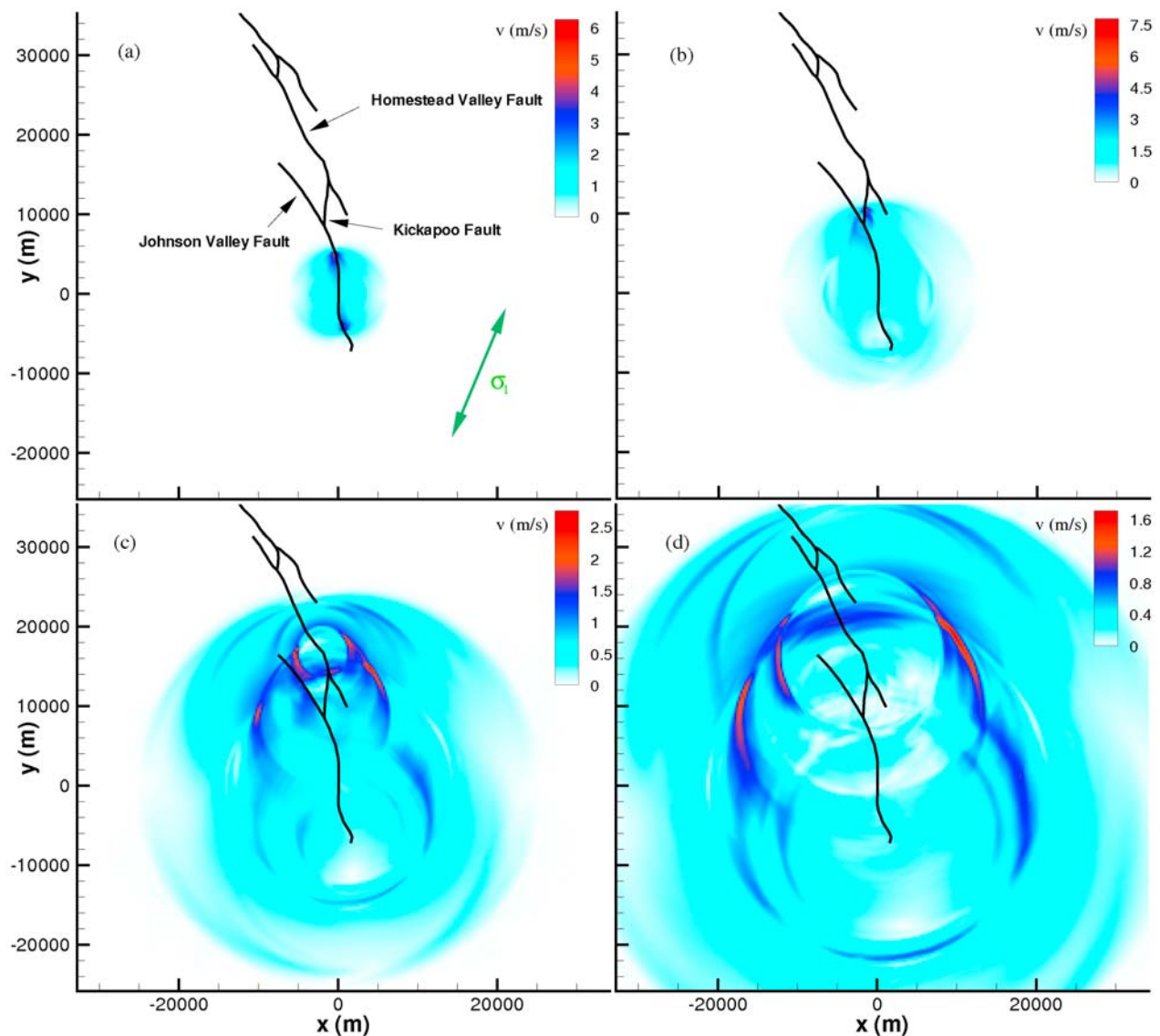


Figure 10. Snapshots of absolute particle velocity for the Landers fault system taken at (a) 1, (b) 2, (c) 4, and (d) 6 s. The direction of the principal stress σ_1 , N22°E, is shown as a green arrow.

[53] The method is currently limited to linear element boundaries, so curved faults can be represented only by piecewise linear segments, and to constant material properties within each element. On the other hand, the ADER-DG method, unlike the SBIE approach, models the whole wavefield and each element can be considered viscoelastic, anisotropic and/or poroelastic (see *de la Puente* [2008] for a review of these cases). Using unstructured meshes can further help to reduce the amount of elements required to mesh very complex structures while its high accuracy could allow the use of coarser spatial samplings than that of other methods and therefore could help ADER-DG to become a competitive tool for dynamic rupture simulations in complicated setups.

[54] The potential of mesh coarsening is twofold. First of all, as has been shown in all cases studied in this paper, coarsening can work as a very effective way to mimic unbounded problems as the domains can be largely extended at the cost of adding a relatively small amount of

elements. This is however largely irrelevant, as other approaches can be used for a similar effect (e.g., perfectly matched layers [*Collino and Tsogka*, 2001; *Komatitsch and Martin*, 2007]). The other potential use, far more unique and

Table 5. Summary of Error Metrics in the 2-D SCEC Benchmark Problem for Different Methods^a

| Method | Rupture Time | | Peak Slip Rate | | Final Slip | |
|------------|--------------|------|----------------|------|------------|------|
| | Order | RMS | Order | RMS | Order | RMS |
| ADER-DG O6 | 2.26 | 0.1% | 1.40 | 9.0% | 1.19 | 0.4% |
| FV | 1.78 | 5.0% | NA | NA | NA | NA |
| SE | 1.88 | 1.0% | NA | NA | NA | NA |
| DFM | 1.53 | 0.8% | 0.68 | 6.5% | 1.28 | 1.3% |
| MOSN | 0.97 | 0.4% | 0.85 | 7.0% | 1.14 | 1.2% |

^aAll RMS values correspond to resolutions of $\Delta x = 100$ m. The FV convergence value has been inferred from Figure 11 of *Benjema et al.* [2007] and is lower than their reported value (1.8 to 2.1). The SE values have been obtained in a subset of integration points and not along the whole fault line. NA, not applicable.

interesting, is the adaptation of the mesh size to the resolution required by the problem locally. Dynamic rupture simulations require a fine sampling of the fault in order to capture the cohesive zone. Applying this fine sampling to the whole wave propagation medium would imply to resolve frequencies much higher than what is typically regarded as useful in strong ground motion records. This warrants a different mesh resolution for the rupture process and for the propagation of the waves. Most mesh-based methods (FD, FE and SE) provide some kind of mesh coarsening strategy. However, a smooth or abrupt transition from a fine to a coarser mesh has to be implemented with care in order to avoid spurious numerical noise or reflections due to the transition [e.g., Moczo *et al.*, 2007]. In contrast, in the presented ADER-DG method using unstructured triangular meshes the mesh coarsening is a pure mesh generation issue and no particular implementation is necessary. The coarsening of the mesh then acts as a filter on the outward propagating wave which leaves the lower frequencies unaffected and does not produce noticeable spurious reflections. We believe this is a remarkable property which rounds up the great potential of the ADER-DG method as a tool to simulate earthquake scenarios with a correct representation of the fault and accurate propagation of the waves through very heterogeneous media.

[55] The obvious next step in the development of the method is to extend the implementation to three dimensions, where the simplicity of tetrahedral meshing will prove more useful for many scenarios and realistic applications. This is especially promising if combined with the so-called local time stepping (LTS) algorithm, that relaxes the CFL stability condition to make it local instead of global [Dumbser *et al.*, 2007]. The reduction of iterations required can considerably speed up the simulations, especially in meshes including elements of very dissimilar sizes. Further improvements will aim at introducing more complex friction laws as well as the heterogeneous Riemann problem, in order to simulate bimaterial ruptures.

10. Conclusion

[56] The ADER-DG method has been successfully adapted to the simulation of dynamic rupture under linear slip weakening friction. We have solved the Riemann problem for elastodynamics to find a linear relation between slip rate and traction at any fault point. This relation is not dependent on the actual choice of the friction law and might be the reason for the remarkably smooth solutions obtained, similar to those obtained with the SBIE method. Such smoothness makes it unnecessary to apply any sort of viscous damping mechanisms in the model. The results obtained for a simple test case show that a scheme of sixth order, i.e., using polynomials of degree five in space and time to represent the unknowns, reaches an error smaller than 0.3% with 1.5 equivalent nodes per cohesive zone size. All orders investigated produce converging solutions for all error measures used: RMS of rupture time, peak slip rate and final slip. The ADER-DG $\mathcal{O}6$ method displays power law exponent on the convergence experiment for the 2-D analog of the SCEC test of 2.26 for rupture time, 1.40 for peak slip rate and 1.19 for final slip. Additionally we have

shown with an application example that the method is very well suited for the simulation of earthquake scenarios involving fault systems which include variations in strike and multiple branches. The method has also been proved to have a very good behavior for meshes with varying element size. The overall effect of a mesh coarsening is the reduction of the amplitude spectra at high frequencies while the low frequencies are preserved. No increase of amplitude in the form of spikes in the spectra is observed for any frequency when comparing results obtained with a coarsened mesh to those obtained on meshes with regular element size. For the 2-D analog of the SCEC test case and for $\mathcal{O}4$ we find the relation between minimum wavelength resolved and element spacing to be $\lambda_{\min} = 1.45 h$. We conclude that the combination of meshing flexibility and high-order accuracy of the ADER-DG method makes it a very interesting tool to study earthquake dynamics on complex fault systems.

[57] **Acknowledgments.** The authors thank the Deutsche Forschungsgemeinschaft (DFG), as the work was supported through the Emmy Noether-program (KA 2281/2-1). We thank Gilbert Brietzke for providing us with the FD and SBIE solutions shown for the 2-D analog of the SCEC test case in section 6 and Cristóbal Castro for some fruitful discussions on the treatment of nonlinear Riemann problems. Steve M. Day and Peter Moczo are also acknowledged for their useful reviews which have helped to clarify and improve the original manuscript.

References

- Aagaard, B. T., T. H. Heaton, and J. F. Hall (2001), Dynamic earthquake rupture in the presence of lithostatic normal stresses: Implications for friction models and heat production, *Bull. Seismol. Soc. Am.*, *91*, 1765–1796, doi:10.1785/0120000257.
- Ampuero, J.-P. (2002), Etude physique et numérique de la nucléation des séismes, Ph.D. thesis, Univ. Denis Diderot Paris 7, Paris.
- Andrews, D. J. (1973), A numerical study of tectonic stress release by underground explosions, *Bull. Seismol. Soc. Am.*, *63*, 1375–1391.
- Andrews, D. J. (1976a), Rupture propagation with finite stress in antiplane strain, *J. Geophys. Res.*, *81*, 3575–3582, doi:10.1029/JB081i020p03575.
- Andrews, D. J. (1976b), Rupture velocity of plane-strain shear cracks, *J. Geophys. Res.*, *81*, 5679–5687, doi:10.1029/JB081i032p05679.
- Andrews, D. J. (1985), Dynamic plane-strain shear rupture with a slip-weakening friction law calculated by a boundary integral method, *Bull. Seismol. Soc. Am.*, *75*, 1–21.
- Andrews, D. J. (1999), Test of two methods for faulting in finite-difference calculations, *Bull. Seismol. Soc. Am.*, *89*, 931–937.
- Aochi, H., and E. Fukuyama (2002), Three-dimensional nonplanar simulation of the 1992 Landers earthquake, *J. Geophys. Res.*, *107*(B2), 2035, doi:10.1029/2000JB000061.
- Aochi, H., R. Madariaga, and E. Fukuyama (2002), Effect of normal stress during rupture propagation along nonplanar fault, *J. Geophys. Res.*, *107*(B2), 2038, doi:10.1029/2001JB000500.
- Benjema, M., N. Glinsky-Olivier, V. M. Cruz-Atienza, J. Virieux, and S. Piperno (2007), Dynamic non-planar crack rupture by a finite volume method, *Geophys. J. Int.*, *171*(1), 271–285, doi:10.1111/j.1365-246X.2006.03500.x.
- Brietzke, G. B., A. Cochard, and H. Igel (2009), Importance of bimaterial interfaces for earthquake dynamics and strong ground motion, *Geophys. J. Int.*, *178*(2), 921–938, doi:10.1111/j.1365-246X.2009.04209.x.
- Castro, C. E., and E. F. Toro (2008), Solvers for the high-order Riemann problem for hyperbolic balance laws, *J. Comput. Phys.*, *227*(4), 2481–2513, doi:10.1016/j.jcp.2007.11.013.
- Cochard, A., and R. Madariaga (1994), Dynamic faulting under rate-dependent friction, *Pure Appl. Geophys.*, *142*, 419–445, doi:10.1007/BF00876049.
- Cochard, A., and J. R. Rice (2000), Fault rupture between dissimilar materials: Ill-posedness, regularization, and slip-pulse response, *J. Geophys. Res.*, *105*, 25,891–25,907, doi:10.1029/2000JB900230.
- Collino, F., and C. Tsogka (2001), Application of the PML absorbing layer model to the linear elastodynamic problem in anisotropic heterogeneous media, *Geophysics*, *66*, 294–307, doi:10.1190/1.1444908.
- Courant, R., K. Friedrichs, and H. Lewy (1928), Über die partiellen Differentialgleichungen der mathematischen Physik, *Math. Ann.*, *100*, 32–74, doi:10.1007/BF01448839.

- Cruz-Atienza, V. M., and J. Virieux (2004), Dynamic rupture simulation of non-planar faults with a finite-difference approach, *Geophys. J. Int.*, *158*(3), 939–954, doi:10.1111/j.1365-246X.2004.02291.x.
- Dalguer, L. A., and S. M. Day (2007), Staggered-grid split-node method for spontaneous rupture simulation, *J. Geophys. Res.*, *112*, B02302, doi:10.1029/2006JB004467.
- Das, S. (1980), A numerical method for determination of source time functions for general three-dimensional rupture propagation, *Geophys. J. R. Astron. Soc.*, *62*, 591–604, doi:10.1111/j.1365-246X.1980.tb02593.x.
- Day, S. M. (1982), Three-dimensional finite-difference simulation of fault dynamics: Rectangular faults with fixed rupture velocity, *Bull. Seismol. Soc. Am.*, *72*, 705–727.
- Day, S. M., and G. P. Ely (2002), Effect of a shallow weak zone on fault rupture: numerical simulation of scale-model experiments, *Bull. Seismol. Soc. Am.*, *92*, 3022–3041, doi:10.1785/0120010273.
- Day, S. M., L. A. Dalguer, N. Lapusta, and Y. Liu (2005), Comparison of finite difference and boundary integral solutions to three-dimensional spontaneous rupture, *J. Geophys. Res.*, *110*, B12307, doi:10.1029/2005JB003813.
- de la Puente, J. (2008), *Seismic Wave Propagation for Complex Rheologies*, VDM, Saarbrücken, Germany.
- de la Puente, J., M. Käser, M. Dumbser, and H. Igel (2007), An arbitrary high order discontinuous Galerkin method for elastic waves on unstructured meshes IV: Anisotropy, *Geophys. J. Int.*, *169*(3), 1210–1228, doi:10.1111/j.1365-246X.2007.03381.x.
- de la Puente, J., M. Dumbser, M. Käser, and H. Igel (2008), Discontinuous Galerkin methods for wave propagation in poroelastic media, *Geophysics*, *73*(5), T77–T97, doi:10.1190/1.2965027.
- Dumbser, M., and M. Käser (2006), An arbitrary high order discontinuous Galerkin method for elastic waves on unstructured meshes II: The three-dimensional case, *Geophys. J. Int.*, *167*(1), 319–336, doi:10.1111/j.1365-246X.2006.03120.x.
- Dumbser, M., M. Käser, and E. F. Toro (2007), An arbitrary high order discontinuous Galerkin method for elastic waves on unstructured meshes V: Local time stepping and p-adaptivity, *Geophys. J. Int.*, *171*(2), 695–717, doi:10.1111/j.1365-246X.2007.03427.x.
- Ely, G., S. M. Day, and J.-B. Minster (2009), A support-operator method for 3D rupture dynamics, *Geophys. J. Int.*, *177*(3), 1140–1150, doi:10.1111/j.1365-246X.2009.04117.x.
- Geubelle, P. H., and J. R. Rice (1995), A spectral method for three-dimensional elastodynamic fracture problems, *J. Mech. Phys. Solids*, *43*, 1791–1824, doi:10.1016/0022-5096(95)00043-I.
- Goto, H., and J. Bielak (2008), Galerkin boundary integral equation method for spontaneous rupture propagation problems: SH-case, *Geophys. J. Int.*, *172*(3), 1083–1103, doi:10.1111/j.1365-246X.2007.03694.x.
- Harris, R. A., et al. (2004), The source physics of large earthquakes: Validating spontaneous rupture methods, *Eos Trans. AGU*, *85*(47), Fall Meet. Suppl., Abstract S12A-05.
- Ida, Y. (1972), Cohesive force across the tip of a longitudinal-shear crack and Griffith's specific surface energy, *J. Geophys. Res.*, *77*, 3796–3805, doi:10.1029/JB077i020p03796.
- Ida, Y. (1973), The maximum acceleration of seismic ground motion, *Bull. Seismol. Soc. Am.*, *63*, 959–968.
- Igel, H., M. Käser, and M. Stuppazini (2008), Simulation of seismic wave propagation in media with complex geometries, in *Encyclopedia of Complexity and System Science*, Springer, New York, in press.
- Kaneko, Y., N. Lapusta, and J.-P. Ampuero (2008), Spectral element modeling of spontaneous earthquake rupture on rate and state faults: Effect of velocity-strengthening friction at shallow depths, *J. Geophys. Res.*, *113*, B09317, doi:10.1029/2007JB005553.
- Käser, M., and M. Dumbser (2006), An arbitrary high order discontinuous Galerkin method for elastic waves on unstructured meshes I: The two-dimensional isotropic case with external source terms, *Geophys. J. Int.*, *166*(2), 855–877, doi:10.1111/j.1365-246X.2006.03051.x.
- Käser, M., M. Dumbser, J. de la Puente, and H. Igel (2007a), An arbitrary high order discontinuous Galerkin method for elastic waves on unstructured meshes III: Viscoelastic attenuation, *Geophys. J. Int.*, *168*(1), 224–242, doi:10.1111/j.1365-246X.2006.03193.x.
- Käser, M., P. Mai, and M. Dumbser (2007b), On the accurate treatment of finite source rupture models using ADER-DG on tetrahedral meshes, *Bull. Seismol. Soc. Am.*, *97*, 1570–1586, doi:10.1785/0120060253.
- Käser, M., V. Herrmann, and J. de la Puente (2008), Quantitative accuracy analysis of the discontinuous Galerkin method for seismic wave propagation, *Geophys. J. Int.*, *173*(3), 990–999, doi:10.1111/j.1365-246X.2008.03781.x.
- Komatitsch, D., and R. Martin (2007), An unsplit convolutional perfectly matched layer improved at grazing incidence for the seismic wave equation, *Geophysics*, *72*(5), SM155–SM167, doi:10.1190/1.2757586.
- Kostrov, B. V. (1964), Self-similar problem of propagation of shear crack, *J. Appl. Math. Mech.*, *28*, 1077–1087, doi:10.1016/0021-8928(64)90010-3.
- Lapusta, N., J. R. Rice, Y. Ben-Zion, and G. Zheng (2000), Elastodynamic analysis for slow tectonic loading with spontaneous rupture episodes on faults with rate- and state dependent friction, *J. Geophys. Res.*, *105*, 23,765–23,789, doi:10.1029/2000JB900250.
- LeVeque, R. (2002), *Finite Volume Methods for Hyperbolic Problems*, Cambridge Univ. Press, Cambridge, U. K.
- Madariaga, R., K. B. Olsen, and R. Archuleta (1998), Modeling dynamic rupture in a 3D earthquake fault model, *Bull. Seismol. Soc. Am.*, *88*, 1182–1197.
- Moczo, P., J. Kristek, M. Galis, P. Pazak, and M. Balazovjech (2007), The finite-difference and finite-element modeling of seismic wave propagation and earthquake motion, *Acta Phys. Slovaca*, *57*(2), 177–406.
- Oglesby, D. D., R. J. Archuleta, and S. B. Nielsen (1998), Earthquakes on dipping faults: the effects of broken symmetry, *Science*, *280*, 1055–1059, doi:10.1126/science.280.5366.1055.
- Oglesby, D. D., R. J. Archuleta, and S. B. Nielsen (2000), The three-dimensional dynamics of dipping faults, *Bull. Seismol. Soc. Am.*, *90*, 616–628, doi:10.1785/0119990113.
- Palmer, A. C., and J. R. Rice (1973), The growth of slip surfaces in the progressive failure of overconsolidated clay slopes, *Proc. R. Soc. London, Ser. A*, *332*, 527–548, doi:10.1098/rspa.1973.0040.
- Rojas, O., S. M. Day, J. Castillo, and L. A. Dalguer (2008), Modelling of rupture propagation using high-order mimetic finite differences, *Geophys. J. Int.*, *172*(2), 631–650, doi:10.1111/j.1365-246X.2007.03651.x.
- Rubin, A., and J.-P. Ampuero (2007), Aftershock asymmetry on a bimaterial interface, *J. Geophys. Res.*, *112*, B05307, doi:10.1029/2006JB004337.
- Toro, E. F. (1999), *Riemann Solvers and Numerical Methods for Fluid Dynamics*, Springer, Berlin.
- Vilotte, J.-P., G. Festa, and J.-P. Ampuero (2006), Dynamic fault rupture propagation using nonsmooth spectral element method, *Eos Trans. AGU*, *87*(52), Fall Meet. Suppl., Abstract S52B-05.

J.-P. Ampuero, Division of Geological and Planetary Sciences, California Institute of Technology, 1200 E. California Boulevard, MC 252-21, Pasadena, CA 91125, USA.

J. de la Puente, Barcelona Center for Subsurface Imaging, Institut de Ciències del Mar, CSIC, Passeig Marítim de la Barceloneta 37-49, Barcelona, Spain. (jdelapuate@cmima.csic.es)

M. Käser, Department of Earth and Environmental Sciences, Section Geophysics Ludwig-Maximilians-University, Theresienstrasse 41, D-80333 Munich, Germany.